A multimodal approach to derive cloud microphysics in deep convective clouds from polarized measurements of the cloudbow

Lea Volkmer[1], Leandro Dörfer[1], and Bernhard Mayer[1]

[1]Meteorologisches Institut, Ludwig-Maximilians-Universität München, Munich, Germany

Correspondence: Lea Volkmer (L.Volkmer@physik.uni-muenchen.de)

Abstract. We present a new method to derive droplet size distributions in clouds consisting of multiple modes using aircraft based polarized measurements of the cloudbow. The retrieval builds onto the existing single mode parametric approach, but allows up to three modes in the droplet size distribution (DSD), where each mode is described by a gamma distribution of effective radius r_{eff} and effective variance v_{eff}. While the DSDs of shallow cumulus or stratiform clouds are often well described by single mode distributions, this does not hold in the presence of drizzle or rain and the measured polarized radiance is not accurately described by a single mode fit. We show that allowing multiple modes in those cases not only improves the fit significantly but also shows good agreement to the Rainbow Fourier Transform (RFT), which derives an arbitrary distribution. The parametric retrieval fits polarized phase functions derived by Mie theory to the measured polarized radiance, such that, for the retrieval of large droplets, new Mie calculations were performed to include effective radii up to $1000\,\mu\text{m}$. In a sensitivity analysis, the uncertainty in the retrieval of large effective radii is tested as the polarized phase functions become less distinct. For effective radii up to about $800\,\mu\text{m}$, the relative mean bias is found to be less than $10\,\%$. The relative noise (standard deviation) increases from about $4\,\%$ for typical cloud droplets of $10\,\mu\text{m}$ to about $30\,\%$ around $500\,\mu\text{m}$ before decreasing again towards even larger effective radii. For the effective variance, increased uncertainties are found both for $r_{\text{eff}} \lesssim 3\,\mu\text{m}$ and $r_{\text{eff}} \gtrsim 200\,\mu\text{m}$. In between, the determination of the effective variance is also possible with an uncertainty of less than $50\,\%$. With the found uncertainties in mind, the new multimode approach is applied to a case study of a deep convective cloud measured during the PERCUSION campaign in 2024 in the vicinity of Barbados, where a rainbow is observed in the RGB image of the camera and also the radar reflectivity shows clear signals of rain. While the single mode retrieval cannot accurately explain the measured signal close to the rainbow observation, the capability of the multimode retrieval to disentangle the signal is demonstrated qualitatively. Furthermore, the individual results from the multimode retrieval are evaluated against the droplet size distributions derived from the Rainbow Fourier Transform (RFT) and similarities are found in most cases, although the results from the RFT show instabilities with negative values in the DSD. Currently, the RFT is only capable to retrieve droplet size distributions with radii up to $100\,\mu\text{m}$, and hence is limited in regions with precipitating droplets. This is where the potential of the multimode approach comes into play as it is capable to detect modes of large effective radii up to $1000\,\mu\text{m}$, which does not only improve the result of a single mode retrieval, but might also allow to learn about physical processes such as rain initiation in deep convective clouds.

Copyright statement. TEXT

1 Introduction

Clouds occur in a large variety almost everywhere on the globe covering on average $67\,\%$ of the surface (King et al., 2013). Hence, they largely influence the Earth's energy budget, having both a warming and a cooling effect. The cooling effect is mainly due to the reflection of solar shortwave radiation back to space, which is determined by the optical properties of clouds, and thus their phase (liquid, ice or mixed-phase) and the size and shape of the cloud particles (e.g. Liou, 2002). Cloud optical properties can be investigated by observing the cloud particles in situ or by remote sensing techniques from ground, aircraft or space using either passive spectral or imaging techniques as well as active radar and lidar techniqiues. Classical passive satellite retrievals are based on a bispectral approach described by Nakajima and King (1990) to derive the cloud effective radius (r_{eff}, Hansen and Travis, 1974) and the cloud optical thickness τ from reflectance measurements in an absorbing and a non-absorbing channel in the visible, near- or shortwave infrared range of the spectrum. While the effective radius is a measure for the effective size of the particles with the observed optical properties, there is no information about the width of the cloud droplet size distribution (CDSD) from the bispectral approach. However, when it comes to cloud microphysical processes, the width of the cloud droplet size distribution is thought to play a crucial role in the onset of precipitation with broader distributions being more favorable for the formation of larger drizzle and rain droplets (e.g., Brenguier and Chaumat, 2001; Chandrakar et al., 2016). From passive remote sensing, information about the cloud droplet size distribution is gained from measurements of the polarized radiance in the scattering angle range between $135\,^\circ$ and $165\,^\circ$, the range of the cloud- and rainbow (e.g. Bréon and Goloub, 1998; Pörtge et al., 2023). In this region, the polarized phase function P_{12} is highly sensitive to the cloud droplet size distribution, and under the assumption of a monomodal gamma distribution as defined by Hansen (1971), the effective radius r_{eff} and the effective variance v_{eff} of the observed cloud area are determined by comparing the measurements to precalculated phase function tables from Mie theory (Mie, 1908). The assumption of a single-mode gamma distribution is widely used (Deirmendjian, 1964; Hansen, 1971; Tampieri and Tomasi, 1976; Alexandrov et al., 2015) and also verified by in situ observations (e.g., Sec. 2.1.4 of Pruppacher and Klett, 2010; Miles et al., 2000).

The polarimetric retrieval has successfully been applied to both space- and airborne measurements, e.g. to measurements of the Polarization and Directionality of the Earth's Reflectances instrument (POLDER; Deschamps et al., 1994; Bréon and Goloub, 1998; Bréon and Doutriaux-Boucher, 2005; Shang et al., 2015), the Research Scanning Polarimeter (RSP; Cairns et al., 1999; Alexandrov et al., 2012a), the Airborne Hyper-Angular Rainbow Polarimeter (AirHARP; Martins et al., 2018; McBride et al., 2020) and the Airborne Multiangle SpectroPolarimetric Imager (AirMSPI ; Diner et al.; Xu et al.). With the launch of NASA's Plankton, Aerosol, Cloud, ocean Ecosystem (PACE) mission in 2024 (Werdell et al., 2026), new spaceborne polarimetric measurements from the Hyper-Angular Rainbow Polarimeter 2 (HARP2) are available, which can be used to derive cloud droplet size distributions (Smith et al., 2026).

Here, we use measurements from the polarization resolving RGB cameras of the airborne spectrometer of the Munich Aerosol Cloud Scanner (specMACS; Weber et al., 2024) to which Pörtge et al. (2023) applied the polarimetric retrieval. The

instrument has been operated onboard the German High-Altitude and LOng range research aircraft (HALO; Krautstrunk and Giez, 2012) during several recent field campaigns, such as the Elucidating the role of clouds-circulation coupling in climate (EUREC^{4}A; Stevens et al., 2021) campaign, the HALO-$(AC)^3$ campaign (Wendisch et al., 2024) and the Persistent EarthCARE underflight studies of the ITCZ and organized convection (PERCUSION; Groß et al., 2026) as part of the larger ORCESTRA campaign (Stevens et al., 2026). Originally, specMACS consisted of two hyperspectral line cameras that measure in the wavelength range between $400\,\mathrm{nm}$ and $2500\,\mathrm{nm}$ (Ewald et al., 2016). Prior to the EUREC^{4}A campaign the instrument has been extended by two downward looking polarization resolving Phoenix 5.0 MP Polarization Model cameras (Pörtge et al., 2023). In 2024, two more sideward-facing polarization cameras were integrated, providing an overall field of view of about $91^\circ \times 220^\circ$ (along $\times$ across track) for the observation of deep convective clouds reaching flight altitudes during the PERCUSION campaign. Each camera covers a field of view of about $91^\circ \times 78^\circ$ and has a resolution of 2448×2048 pixels (along $\times$ across track, Weber et al., 2024). Moreover, the cameras provide simultaneous measurements at a frame rate of $5 - 8\,\mathrm{Hz}$ resulting in a high temporal resolution. Together, this allows to aggregate the scattered polarization signal from cloud targets at a spatial resolution of about $100 \times 100\,\mathrm{m}$ and an angular resolution of 0.3° (Pörtge et al., 2023).

Until now, the polarimetric retrieval from specMACS has mainly been applied to boundary layer clouds. During the EUREC^{4}A campaign, the retrieval was used on non-precipitating shallow cumulus clouds (Pörtge et al., 2023; Pörtge, 2024) and Weber et al. (2026, 2025a) had a look on the cloud microphysics of arctic mixed-phase clouds observed in marine cold air outbreaks during the HALO-$(AC)^3$ campaign. In those cases, where the assumption of a monomodal gamma distribution holds for the liquid cloud phase (Alexandrov et al., 2015), Volkmer et al. (2024b) performed an analysis of the retrieval uncertainties based on synthetic model simulations and found a mean bias $\pm$ standard deviation of $(-0.2 \pm 1.30)\,\mu\mathrm{m}$ for the retrieved effective radius. For the effective variance, an uncertainty of (0.02 ± 0.05) was found.

However, the flights of the recent PERCUSION campaign targeted the Intertropical Convergence Zone (ITCZ), which is characterized by a trimodal distribution of cloud types, namely shallow cumulus, congestus and cumulonimbus (Johnson et al., 1999). During the first part of the campaign from 09 August to 06 September 2024, HALO was based in Sal, Cape Verde in the eastern tropical Atlantic before being transferred to Barbados to target the western part of the tropical Atlantic basin from 06 to 30 September 2024. In both parts, all of the three kinds of tropical clouds defined by Johnson et al. (1999) were identified and next to the cloudbow, the much more intense rainbow could be observed in coexistence in particular on the lower cloud sides where precipitation falls out. In this case, the assumption of a single mode gamma distribution does not hold any longer. Even though the rainbow is in general much narrower and more intense than the cloudbow, the superposition of the two signals causes erroneous results in the single mode retrieval, usually in terms of an overestimation of the actual cloud effective radius.

One method, which does not require any a priori assumption on the shape of the CDSD, is the so-called Rainbow Fourier Transform (RFT; Alexandrov et al., 2012b). It is based on an integral transform that decomposes the observed signal into a sum of pre-calculated phase functions over size bins. Alexandrov et al. (2015) observed, that the resulting droplet size distribution (DSD) from the RFT is usually well described by a superposition of multiple single mode gamma distributions, such that they introduced a method to decompose the DSD into several modes, each defined by an effective radius and variance. However, one issue of the RFT is that the derived DSDs can show artifacts caused by the non-orthogonality of the polarized phase functions.

This is corrected by an universal correction function independent of the actual size distribution (Alexandrov et al., 2012b). The RFT has further been developed on a database of equally spaced ($0.5\,\mu\mathrm{m}$) polarized phase functions from Mie theory integrated over a very narrow triangular size distribution of width $0.1\,\mu\mathrm{m}$ up to a maximum radius of $100\,\mu\mathrm{m}$. Hence, the resulting size distributions $n(r)$ fulfill the condition $n(r > 100\,\mu\mathrm{m}) = 0$ per definition, while actual rain droplets have sizes up to several millimeters (Pruppacher and Klett, 2010, Sec. 2.1.6). Therefore, using the RFT in cases where cloud and rain droplets coexist would require a huge database of polarized phase functions calculated from Mie theory, not only in terms of calculated radii but also in terms of the angular resolution (0.2° in the case of Alexandrov et al. (2012b)), since the number of oscillations increases for larger radii. While the RFT remains formally valid in case of large radii, its practicability deteriorates for our applications.

To this end, we introduce a new multimodal fitting approach in this paper analogue to the polarimetric retrieval, but allowing the appearance of multiple (single-mode) gamma distributions. We start in Sec. 2 with the description of the retrieval algorithm and Sec. 3 shows an example on real measurements. Further, Sec. 3.1 includes a comparison of individually measured cloud targets to the existing RFT. Finally, Sec. 4 discusses the introduced method and reveals how this can be used to investigate scientific questions.

2 Retrieval description

This sections gives a detailed description of the presented multimodal cloud droplet size distribution retrieval. We start with the theoretical basis and the mathematical formulation of the problem, followed by the actual numerical implementation.

2.1 Theoretical framework

The scattering of electromagnetic waves on spherical particles is fully described by Mie theory (Mie, 1908). In general, for radiation traveling along the positive z-axis the scattered electric field vector $\boldsymbol{E}_{\mathrm{sc}} = (E_l, E_r)^T_{\mathrm{sc}}$ is related to the incoming electric field vector $\boldsymbol{E}_{\mathrm{in}} = (E_l, E_r)^T_{\mathrm{in}}$ by the scattering amplitude matrix (e.g., Bohren and Huffman, 1998, Sec. 3.2)

$$\begin{pmatrix} E_l \\ E_r \end{pmatrix}_{\mathrm{sc}} = \frac{e^{ik(R-z)}}{-ikR} \begin{pmatrix} S_2 & S_3 \\ S_4 & S_1 \end{pmatrix} \begin{pmatrix} E_l \\ E_r \end{pmatrix}_{\mathrm{in}} . \tag{1}$$

The state of the polarization of the electromagnetic radiation is conveniently described in terms of the Stokes vector

$$\boldsymbol{I} = \begin{pmatrix} I \\ Q \\ U \\ V \end{pmatrix} = \begin{pmatrix} \langle E_l E_l^* + E_r E_r^* \rangle \\ \langle E_l E_l^* - E_r E_r^* \rangle \\ \langle E_l E_r^* + E_r E_l^* \rangle \\ i \langle E_l E_r^* - E_r E_l^* \rangle \end{pmatrix} \tag{2}$$

and the incoming $\boldsymbol{I}_{\mathrm{in}}$ and outgoing $\boldsymbol{I}_{\mathrm{sc}}$ Stokes vectors are related by the 4×4 scattering phase matrix $\boldsymbol{P}$

$$\boldsymbol{I}_{\mathrm{sc}} = \frac{\sigma_{\mathrm{sca}}}{4\pi R^2} \boldsymbol{P} \boldsymbol{I}_{\mathrm{in}}, \tag{3}$$

where σ_{sca} is the scattering cross-section. $\boldsymbol{P}$ can be calculated from the amplitude scattering matrix, which is diagonal for spherical particles ($S_3 = S_4 = 0$) due to symmetry, such that $\boldsymbol{P}$ is fully described by four elements, namely P_{11}, P_{12}, P_{33} and P_{34}.

The existing polarimetric retrievals of the CDSD use that the polarized reflectance $R_p = -\frac{\pi Q}{\mu_s I_0}$ is proportional to the measured component Q of the scattered Stokes vector in the scattering plane when $U \approx 0$ and that in turn, $R_p \propto Q \propto P_{12}$ (e.g., Bréon and Goloub, 1998; Alexandrov et al., 2012a; Pörtge et al., 2023). Here, μ_s is the cosine of the solar zenith angle and I_0 is the incoming extraterrestrial solar irradiance. P_{12} is for spherical particles calculated from the elements S_1 and S_2 of the amplitude scattering matrix as

$$P_{12} = \frac{2\pi}{\sigma_{\text{sca}} k^2} \left(|S_2|^2 - |S_1|^2 \right). \tag{4}$$

Following Alexandrov et al. (2012b), the average polarized phase function $\bar{P}_{12}(\theta)$ in terms of the scattering angle θ for an arbitrary normalized droplet size distribution $n(r)$ can be written as

$$\bar{P}_{12}(\theta) = \frac{\int_0^\infty \sigma_{\text{sca}}(r) P_{12}(r,\theta) n(r) dr}{\int_0^\infty \sigma_{\text{sca}}(r) n(r) dr}. \tag{5}$$

In case of the polarimetric retrievals, $n(r)$ is often assumed to have the form of a monomodal gamma distribution which, as defined by Hansen (1971), can be written as

$$n(r) = n_0 r^{(1-3v_{\text{eff}})/v_{\text{eff}}} e^{-r/(r_{\text{eff}} v_{\text{eff}})}. \tag{6}$$

Hereby, r_{eff} is the area-weighted mean or effective radius

$$r_{\text{eff}} = \frac{\int_0^\infty r \pi r^2 n(r) dr}{\int_0^\infty \pi r^2 n(r) dr} \tag{7}$$

and v_{eff} is the dimensionless effective variance

$$v_{\text{eff}} = \frac{\int_0^\infty (r - r_{\text{eff}})^2 \pi r^2 n(r) dr}{r_{\text{eff}}^2 \int_0^\infty \pi r^2 n(r) dr}. \tag{8}$$

As first introduced by Bréon and Goloub (1998) and following the notation of Pörtge et al. (2023), a general fit function of the form

$$Q_{\text{fit}} = A \cdot P_{12}[r_{\text{eff}}, v_{\text{eff}}](\theta) + B \cdot \cos^2(\theta) + C \tag{9}$$

is used to determine the best fitting effective radius and variance for the observed polarized radiance under the assumption of a single mode gamma distribution. The parameters A, B and C are fitting parameters.

As already observed by Alexandrov et al. (2015) from the application of the Rainbow Fourier Transform, the DSD can have a pronounced multimodal shape and decomposed the retrieved DSD into several single-mode gamma distributions. Assuming now that the DSD can be written as a superposition of M single-mode distributions $n(r) = \sum_{i=1}^{M} n_i(r)$, we can rewrite Eq. (5) as

$$\bar{P}_{12}(\theta) = \sum_{i=1}^{M} \frac{\int_0^\infty \sigma_{\text{sca}}(r) n_i(r) dr}{\int_0^\infty \sigma_{\text{sca}}(r) n(r) dr} \frac{\int_0^\infty \sigma_{\text{sca}}(r) P_{12}(r,\theta) n_i(r) dr}{\int_0^\infty \sigma_{\text{sca}}(r) n_i(r) dr} \equiv \sum_{i=1}^{M} \frac{\beta_{\text{ext},i}}{\beta_{\text{ext,tot}}} \bar{P}_{12}^i \equiv \sum_{i=1}^{M} f_{\beta,i} \bar{P}_{12}^i. \tag{10}$$

Hence, the observed scattered polarized radiation can be expressed in terms of a superposition of the polarized radiation scattered by the single distributions. The fraction that the individual size distribution contributes to the total signal $f_{\beta,i}$ equals hereby the fraction of the extinction coefficient $\beta_{\text{ext},i}$ to the total extinction coefficient $\beta_{\text{ext,tot}}$ when absorption is negligible. Note that this holds in general for any arbitrary shape of the individual size distributions $n_i(r)$. However, assuming that the individual distributions obey the shape of single-mode gamma distributions, we introduce the fit function in the presence of multiple modes in accordance to Eq. (9) as

$$Q_{\text{fit}} = \sum_{i=1}^{M} A_i \cdot P_{12}^{i}[r_{\text{eff},i}, v_{\text{eff},i}](\theta) + B \cdot \cos^2(\theta) + C. \tag{11}$$

Comparing equations (10) and (11) suggests that the fit factors $A_i \propto f_{\beta,i}$, but they incorporate for the conversion between the phase matrix elements to the measured radiance Q, as A does in Eq.(9). For example, we do not convert the measured Q to the polarized reflectance. Further, the measured polarization can be reduced due to ice or aerosol particles within or above the cloud target.

This allows to define a "signal fraction" f_A as the normalized fitted amplitude of each mode

$$f_{A,i} = \frac{A_i}{A_{\text{tot}}}, \;\; A_{\text{tot}} = \sum_{i=1}^{M} A_i \tag{12}$$

where A_i refers to the fit parameter of Eq.(11). A_{tot} is hereby the normalization factor which ensures that $\sum_{i=1}^{M} f_{A,i} = 1$. Provided that the multiplicative scaling factor within A_i is the same for all modes, we get

$$f_{A,i} = \frac{A_i}{A_{\text{tot}}} \approx f_{\beta,i} = \frac{\beta_{\text{ext},i}}{\beta_{\text{ext,tot}}} = \frac{\tau_i}{\tau_{\text{tot}}}, \tag{13}$$

where $f_{\beta,i}$ is the same factor as in Eq.(10) and τ_i and τ_{tot} denote the optical thickness of mode i and the total optical thickness, respectively. The assumption of a common multiplicative scaling factor is motivated by the saturation of the polarized cloud signal at sufficiently large liquid optical thicknesses, typically around $3-5$ (Weber et al., 2025b). Then, the scaling factor may become less sensitive to further increases in optical thickness and is mainly determined by the conversion from polarized radiance (Q) to reflectance and external factors, such as depolarizing aerosol or ice particles above or within the clouds, respectively and the normalization of the phase functions. Further, we assume here that we observe a homogeneously mixed target, such that $\beta_{\text{ext},i}/\beta_{\text{ext,tot}} = \tau_i/\tau_{\text{tot}}$ holds.

Moreover, the signal fraction can be used to calculate a fraction with respect to the liquid water content f_{LWC} and the droplet number concentration f_{N}. Using that the extinction efficiency $Q_{\text{ext}} \approx 2$ for particles that are much larger than the wavelength (Hansen and Travis, 1974), the definition of the r_{eff} after Eq.(7), the extinction coefficient

$$\beta_{\text{ext}} = \int_0^\infty Q_{\text{ext}}(r)\pi r^2 n(r) dr \tag{14}$$

and the liquid water content

$$\text{LWC} = \frac{4}{3}\pi\rho \int_0^\infty r^3 n(r) dr = \frac{4}{3}\pi\rho N \bar{r}_v^3, \tag{15}$$

where N is the droplet number concentration and ρ is the water density, the extinction coefficient can be approximated as

$$\beta_{\text{ext}} \approx \frac{3\text{LWC}}{2r_{\text{eff}}}. \tag{16}$$

Further, Eq.(15) can be written in terms of the effective radius as

$$\text{LWC} = \frac{4}{3}\pi k r_{\text{eff}}^3 \rho N, \tag{17}$$

where we used that $k = (1 - v_{\text{eff}})(1 - 2v_{\text{eff}})$ connects the mean volume radius $\bar{r}_v^3 = k r_{\text{eff}}^3$ to the effective variance of the gamma distribution. Hence, we can derive the liquid water content fraction as

$$f_{\text{LWC},i} = \frac{\text{LWC}_i}{\text{LWC}} = \frac{f_{A,i} \cdot r_{\text{eff,i}}}{\sum_{i=0}^{3} f_{A,i} \cdot r_{\text{eff,i}}} \tag{18}$$

and the fraction of the droplet number concentration as

$$f_{N,i} = \frac{N_i}{N_{\text{tot}}} = \frac{f_{A,i}/(k_i \cdot r_{\text{eff,i}}^2)}{\sum_{i=0}^{3} f_{A,i}/(k_i \cdot r_{\text{eff,i}}^2)}. \tag{19}$$

2.2 Phase functions for large droplets

While Mie theory provides an exact solution of the Maxwell equations for the scattering of light by spherical particles, it is represented by an infinite series of Legendre Polynomials. Thus, for practical applications, the series has to be truncated when a reasonable accuracy has been reached. In general, the Mie solution depends on the ratio between the radius and the wavelength λ of the scattered light, which is in most applications expressed in terms of the size parameter x defined as

$$x = \frac{2\pi r}{\lambda}. \tag{20}$$

The series of Legendre Polynomials converges approximately when $N_l \gtrsim x$ (Grandy, 2000, Sec. 3.4, p. 102), where N_l is the number of calculated terms. Hence, calculations become more expensive the larger the size parameter.

For our application, we have to extend the existing phase function table generated by Pörtge et al. (2023) to effective radii of rain droplet size distributions (RDSD). Therefore, we assume that RDSDs can be described in terms of gamma distributions to be consistent with the existing phase function table. A widely used assumption for the rain droplet size distribution is the Marshall-Palmer distribution (Marshall and Palmer, 1948; Pruppacher and Klett, 2010, Sec. 2.1.6), which follows an exponential relationship between the droplet number concentration N_D and the droplet diameter $D = 2r$:

$$N_D(D) = N_0 e^{-\Lambda D} = N_0 e^{-2\Lambda r} \tag{21}$$

Marshall and Palmer (1948) further found N_0 to be constant with $N_0 = 8{\cdot}10^4\,\text{m}^{-3}\text{cm}^{-1}$ and the slope parameter $\Lambda = 41R^{-0.21}$ to vary with the rainfall rate R in mmhr^{-1}. Since this is a special case of the modified gamma distribution in Eq.(6) with $v_{\text{eff}} = 1/3$ and $\Lambda = 1/(2r_{\text{eff}}v_{\text{eff}})$, the phase function table was not only extended in terms of the effective radius, but also by two further effective variances $v_{\text{eff}} = 1/3$ and $v_{\text{eff}} = 0.4$. Multiple studies, such as Ulbrich (1983) and Willis and Tattelman

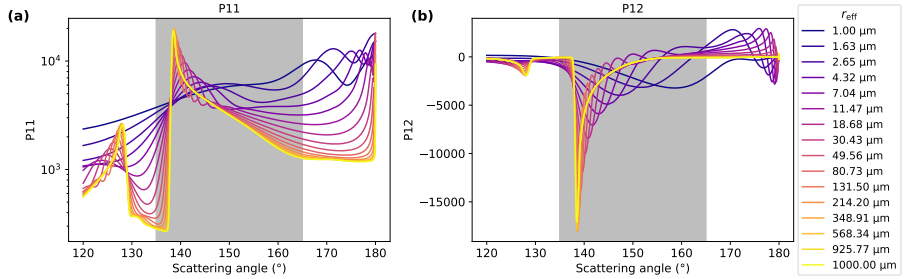


Figure 1. Phase matrix components P_{11} in **(a)** and P_{12} in **(b)** of the extended phase function table in the scattering angle range between $120°$ and $180°$ for different effective radii between $1\,\mu m$ and $1000\,\mu m$ and a constant effective variance of 0.1 integrated for the green channel of the polarization cameras of the specMACS instrument. The gray shaded area marks the scattering angle region between $135°$ and $165°$ where the polarimetric cloudbow retrieval is performed (Pörtge et al., 2023; Alexandrov et al., 2012a).

(1989) have shown that the use of the gamma distribution in a more general form can be used to describe RDSDs fairly well and further justifies our assumption of underlying gamma distributions for larger rain droplet size spectra.

For our extended phase function table, we performed Mie calculations using the MIEV0 Code by Wiscombe (1980), which is implemented into the Mie tool that comes with the library for radiative transfer (libRadtran; Mayer and Kylling, 2005; Emde et al., 2016). Since we want to use the phase function table for a retrieval based on measurements of the polarization resolving RGB cameras of specMACS, the phase function calculations were performed for the wavelength range between $380\,nm$ and $710\,nm$ and integrated over the spectral response function of the cameras (Weber et al., 2024). Our extended phase function table includes now 143 effective radii from $1\,\mu m$ to including $1000\,\mu m$ with $r_{\text{eff},i+1} = r_{\text{eff},i} \cdot 1.05$ for the same 16 effective variances between 0.01 and 0.325 as used by Pörtge et al. (2023) and the two new effective variances $1/3$ and 0.4.

Figure 1 shows the phase matrix components P_{11} and P_{12} in the scattering angle range between $120°$ and $180°$ integrated for the green channel of the RGB polarization cameras of specMACS for an effective variance of $v_{\text{eff}} = 0.1$ and different effective radii between $1\,\mu m$ and $1000\,\mu m$ (every 10th radius of the extended phase function table). The gray shaded area in both panels marks the region of the cloud- (and rainbow) between $135°$ and $165°$ scattering angles which has been used for the polarimetric retrievals of CDSDs (e.g, Pörtge et al., 2023; Alexandrov et al., 2012a). It can be seen, that in particular the polarimetric phase functions P_{12} split up in that regime for the different effective radii and the minimum moves towards lower scattering angles for larger effective radii. However, it also becomes clear that there is less sensitivity for larger effective radii. We will investigate this in more detail in Sec. 2.4. Next to the cloud- and rainbow, we can also see the second order rainbow as a secondary maximum in P_{11} and a secondary minimum in P_{12} between $120°$ and $130°$, which becomes more pronounced for larger effective radii. In between the two rainbows, Alexander's dark band is clearly visible for larger radii. Around $180°$, the backscatter glory can be identified, which has also been used for remote sensing of cloud droplet size distributions (Mayer et al., 2004).

Figure 2 shows the dependence of the polarized phase function P_{12} on the effective variance for four different effective radii of $1.00\,\mu m$ (panel **a**), $9.91\,\mu m$ (panel **b**), $98.13\,\mu m$ (panel **c**), and $1000\,\mu m$ (panel **d**) in the cloud-/ rainbow range between

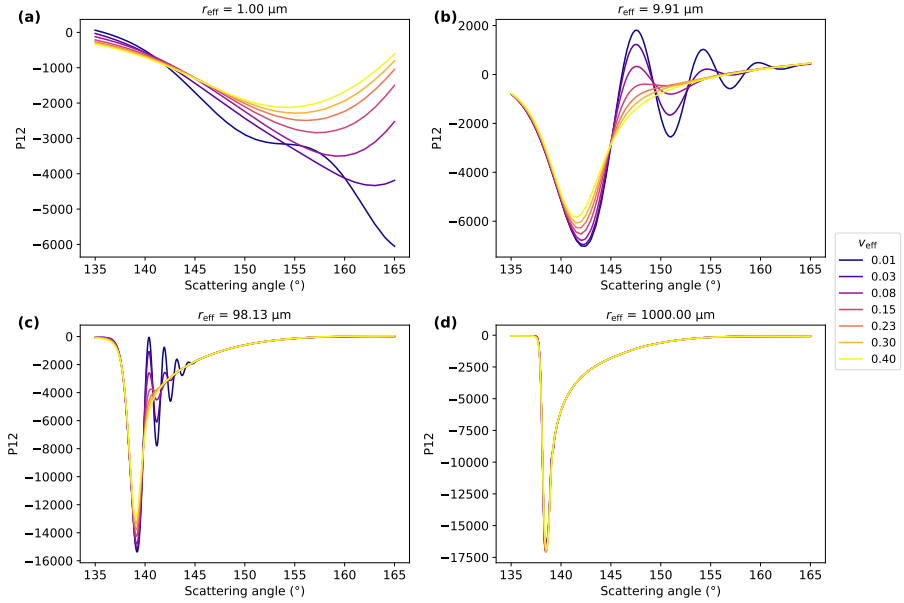


Figure 2. Dependence of the polarized phase function P_{12} on the effective variance for four different effective radii: $1.00\,\mu m$ **(a)**, $9.91\,\mu m$ **(b)**, $98.13\,\mu m$ **(c)**, and $1000\,\mu m$ **(d)**.

$135°$ and $165°$. While the phase functions split up well for $1.00\,\mu m$, $9.91\,\mu m$, and $98.13\,\mu m$, hardly any difference can be seen for $1000\,\mu m$. For $9.91\,\mu m$ and $98.13\,\mu m$, the polarized phase functions show next to the mostly aligned major minimum so-called supernumerary bows for the smaller the effective variances. In contrast, the phase functions for $1.00\,\mu m$ show significant differences between the effective variances as well, however, the minimum shifts clearly towards larger scattering angles for smaller effective variances. For $v_{eff} = 0.01$, the major minimum is not even visible in the range of the cloudbow. Since shifts in the minimum occur also due to changes in the effective radius, there might be less sensitivity in the fit also for very small radii. Due to the indifference of P_{12} for different effective variances at $1000\,\mu m$, it can be expected that large uncertainties in v_{eff} might occur at those values. As mentioned before, this will be investigated further in Sec. 2.4.

The motivation for the implementation of the multimode retrieval can be seen in Fig. 3. It illustrates the effect on the polarized phase function when two modes coexist in the droplet size distribution for a first mode with $r_{eff,1} = 9.91\,\mu m$ and a second one with $r_{eff,2} = 98.13\,\mu m$. Different fractions that the individual modes contribute to the overall signal were chosen with $f_1 \in \{1.0, 0.8, 0.5, 0.3, 0.0\}$ and $f_2 = 1 - f_1$. The existence of a second mode in the DSD changes the polarized phase function significantly, and hence would bias a retrieval that assumes a single mode gamma distribution.

2.3 Retrieval algorithm

The retrieval algorithm is based on the aggregated angular radiance measurements in the scattering angle range between $135°$ and $165°$ described by Pörtge et al. (2023) and uses the single mode results as a starting point. The results from the single

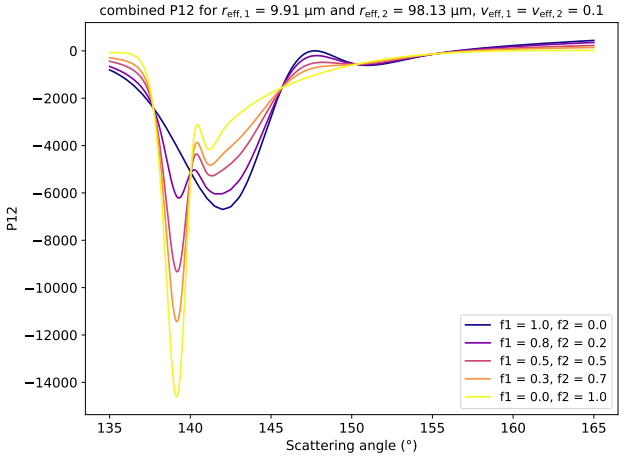


Figure 3. Effect of the coexistence of two modes in the droplet size distribution on the polarized phase functions for $r_{\text{eff},1} = 9.91\,\mu\text{m}$ and $r_{\text{eff},2} = 98.13\,\mu\text{m}$. For both modes an effective variance of $v_{\text{eff}} = 0.1$ was chosen. Different fractions for the individual modes were chosen with $f_1 \in \{1.0, 0.8, 0.5, 0.3, 0.0\}$ and $f_2 = 1 - f_1$.

mode fit contain several quality measures which evaluate the quality of the fit (Pörtge et al., 2023): The root mean square error (RMSE, Eq.(7) in Pörtge et al. (2023))

$$\text{RMSE} = \sqrt{\frac{1}{N}\sum_{i=0}^{n}(Q_{\text{fit}}(\theta_i) - Q_{\text{meas}}(\theta_i))^2} \tag{22}$$

and the quality index (QI, Eq.(8) in Pörtge et al. (2023))

$$\text{QI}^2 = \frac{A^2(\langle P_{12}^2\rangle - \langle P_{12}\rangle^2)}{\text{RMSE}^2}. \tag{23}$$

As in Eq.(9), θ denotes the scattering angle and A is the fit parameter that scales the polarized phase functions to the measured amplitude of the cloudbow. Cloud targets of the single mode fit results are not considered for further analysis, when RMSE $>$ 2.5 and QI < 4 (Pörtge et al., 2023). Those targets, which do not fulfill the quality measures of the single mode fit are then used as an input for the multimode retrieval. However, targets where $A < 0.001$ and QI < 1.5 are not considered, since the signals do not contain a lot of information, e.g. due to ice, shadows or ocean influence.

While the single mode fit function from Eq.(9) has five free parameters for the fit (A, B, C, r_{eff}, and v_{eff}), every additional mode in the fit function after Eq.(11) adds another three free parameters to the parameter space, because the background B and C is fitted only once. Hence, it would be ambiguous to search the whole lookup table (LUT) for each mode and we decided on a strategy, which subsequently adds modes to the fit and searches the LUT in three different stages. First, an independent one-mode search is performed within the multimode retrieval by performing a coarse search through the LUT, which keeps every sixth effective radius and effective variance values. Since the fit is much more sensitive to r_{eff} than v_{eff}, we look for the best fitting effective radii for the central effective variance of the kept values first. The results for the five best effective radius fits are

then combined with all possible effective variances to find again the five best candidates. Then, the fit is refined in a secondary coarse search around these best results from the first coarse search, which takes every second r_{eff} and v_{eff} in a window that includes the two neighbors of the coarsened LUT in both dimensions (r_{eff} and v_{eff}) around the found result into account. Again, the five best candidates from the second stage fit are kept, to perform a final search, which takes all candidates within a window of size two (± 2 neighbors) around those results. Hereby, the result of the first mode found can be interpreted as the dominant mode generating the signal and does not resemble an average over the whole multimodal distribution, as already observed by Alexandrov et al. (2012a).

The result of the first mode serves as a starting point for sequentially adding up to a predefined maximum number of modes n_m. For the new mode, the fit strategy described above is repeated, while the results for the r_{eff} and v_{eff} of the single best fit from the preceding step are used as centers for local search windows. Hence, when adding a second mode, the possible r_{eff} and v_{eff} values of the coarsened LUT are combined with the neighboring values of the LUT of the best r_{eff} and v_{eff} of the first mode. For each combination, the fit parameters A_i, B, and C are refitted to minimize the objective function (here: RMSE), and the best result is kept to perform the secondary coarse search and the fine search with the newly added mode.

Modes are added until either the predefined maximum number of modes is reached or the newly obtained fit satisfies the RMSE threshold (currently 1.2) for all fitted color channels. A newly added mode is accepted only when the objective function does not worsen and the fitted mode amplitudes are positive for all fitted color channels. If the new fit worsens the objective for any of the color channels, the preceding best valid fit is retained.

Because different combinations of phase functions can produce similar angular radiance curves, the multimode inverse problem may admit several comparably good solutions. Hence, it should be mentioned that the result might describe a local minimum rather than the global minimum which could lead to errors in the resulting droplet size distributions. Further, the resulting solution is conditional on the LUT, search-window strategy, objective function, and positivity constraints. However, first applications of the current fit strategy show promising results, which are presented in Sec. 3.

Afterwards, the quality of the results of the multimode fit can still be ensured by applying a threshold filter as for the single mode retrieval. Next to the RMSE, we define the quality index QI for a multimodal fit analog to the quality index for the single mode fit from Eq.(23) as

$$\text{QI}^2 := \frac{\text{Var}(\sum_{i=1}^{M} A_i P_{12}^i)}{\text{RMSE}^2} = \frac{\left\langle (\sum_{i=1}^{M} A_i P_{12}^i))^2 \right\rangle - \left\langle \sum_{i=1}^{M} A_i P_{12}^i) \right\rangle^2}{\text{RMSE}^2}. \tag{24}$$

Similar to the goodness thresholds for the single mode fit, we filter targets when RMSE < 2.5 and QI > 4. The individual steps of the retrieval algorithm and the fit strategy are summarized in Fig. 4.

2.4 Sensitivity of the single mode retrieval to large droplets

Figure 1 shows that the phase functions for larger droplets do not split up as much as the phase functions for the well tested smaller droplets in the cloudbow region. Hence, the first question to be answered is the sensitivity of the fit to larger droplets. To this end, we added random measurement noise equivalent to the noise in real measurements of the specMACS polarization cameras to the phase functions in the LUT and generated a data set which includes several targets for each $(r_{\text{eff}}, v_{\text{eff}})$ pair. The

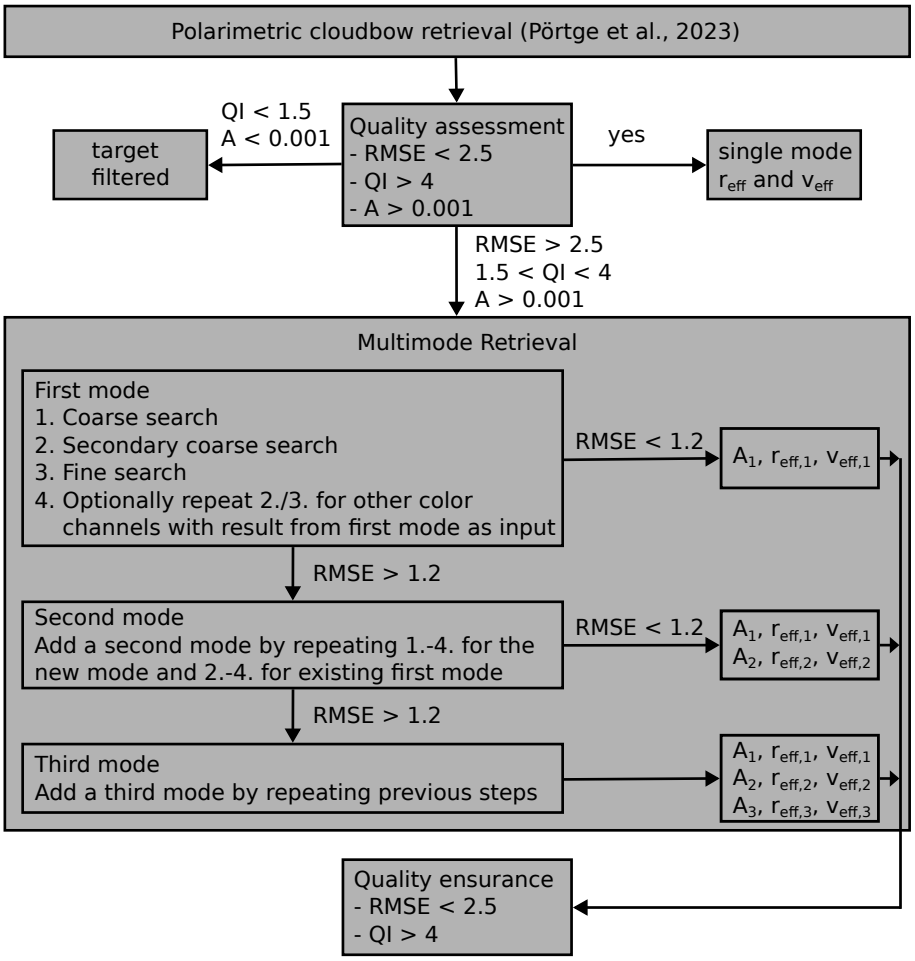


Figure 4. Schematic overview of the retrieval algorithm and fit strategy.

fit routine described in Sec. 2.3 was applied to the measurement resembling data set for a maximum number of modes $n_m = 1$ allowing to test the sensitivity of a single mode fit dependent on the actual effective radius and variance. The results are shown in Fig. 5. In panel **(a)**, a larger spread of the derived effective radius can be seen both towards small effective radii smaller than about $2\,\mu\mathrm{m}$ and as expected also towards effective radii larger than about $200\,\mu\mathrm{m}$. In **(b)**, the comparison between the actual input effective variance and the derived effective variance is plotted, showing a spread for all values. While the mean follows the 1:1 line well, a slight overestimation can be seen for small effective variances and an underestimation for larger effective variances, which is due to the end of the LUT. Further, it can be seen that the retrieved effective variances accumulate both in the smallest ($v_{\mathrm{eff}} = 0.01$) and the largest ($v_{\mathrm{eff}} = 0.4$) effective variance bins, which is mainly due to insensitivities of the phase functions for large effective radii as seen in Fig. 2.

In **(c)** and **(d)**, the absolute (black, left axis) and the relative (red, right axis) mean biases are shown with respect to the input effective radius and variance respectively. The mean bias of the effective radius remains approximately zero for effective radii

up to $200\,\mu m$ which is consistent with the findings from panel **(a)** and also holds for the relative mean bias, although the relative mean bias is increased for $r_{\text{eff}} < 2\,\mu m$ as seen before. For radii between $200\,\mu m$ and about $700\,\mu m$, the mean bias increases to about $+20\,\mu m$ around $500\,\mu m$, before it falls off to negative values down to about $-175\,\mu m$ at $1000\,\mu m$. The overestimation for $r_{\text{eff}} < 2\,\mu m$ and the underestimation for $r_{\text{eff}} \gtrsim 700\,\mu m$ might also be related to the fact that they are close to the borders of the LUT, such that potential errors are always positive or respectively negative. Altogether, it can be concluded that the effective radius can be determined with an accuracy better than $10\,\%$ between about $1.5\,\mu m$ and $800\,\mu m$ and hence, fulfills the requirement determined by Mishchenko et al. (2004) for the r_{eff} of liquid droplet size distributions to monitor the long-term aerosol and cloud forcing from space. For the bias of the effective variance shown in panel **(d)**, a steady decrease towards larger v_{eff} can be seen. While the effective variance is overestimated for $v_{\text{eff}} \lesssim 0.15$, it is underestimated for values above 0.15. The overestimation at small effective variances results in a relative bias of up to about 2, with a fast decrease down to about 0.2 at $v_{\text{eff}} = 0.05$. At the largest effective variance of $v_{\text{eff}} = 0.4$ an underestimation of about -0.07 or $-20\,\%$ is found. Again, it should be kept in mind that overestimates at small effective variances and underestimates at large v_{eff} might be caused by reaching the borders of the LUT. Compared to the accuracy requirements determined by Mishchenko et al. (2004) of 0.05 or $50\,\%$, the requirements are met for all effective variances, either because of their low absolute or relative bias.

The same is shown for the standard deviation in panel **(e)** and **(f)**. As denoted before, the standard deviation of the derived effective radius is large for very small effective radii ($r_{\text{eff}} \ll 2\,\mu m$), which is mostly due to single outliers. While it drops to a minimum of about $0.1\,\mu m$ at $r_{\text{eff}} \approx 3\,\mu m$, it steadily increases for larger r_{eff} up to nearly $200\,\mu m$ for $r_{\text{eff}} \gtrsim 500\,\mu m$. However, this means that the relative standard deviation stays below about 0.4 for all r_{eff} except for the very small values close to about $1\,\mu m$. The standard deviation of the derived effective variance generally increases for larger input effective variances from about 0.06 to about 0.10 for $v_{\text{eff}} \gtrsim 0.3$. However, the relative standard deviation steadily decreases for larger v_{eff} with values below 0.5 for $v_{\text{eff}} \gtrsim 0.15$.

Volkmer et al. (2024b) performed an extensive study on the accuracy of the single mode polarimetric retrieval applied to measurements of the specMACS instrument using 3-D radiative transfer simulations of a field of shallow cumulus clouds. They found an uncertainty in the effective radius of $(-0.17 \pm 1.30)\,\mu m$, which corresponds to a relative mean bias of less than $2\,\%$ when compared to the average radius of $10.49\,\mu m$ expected from the model data. While the values found were averaged for all effective radii between $1\,\mu m$ and about $40\,\mu m$ (the values included in the existing LUT for the single mode retrieval), they compare well to the values found from Fig. 5c. With regard to the effective variance, Volkmer et al. (2024b) found an uncertainty of (0.02 ± 0.05), which corresponds to a relative mean bias of $15\,\%$ at an average expected effective variance of 0.14. Note that the simulations did not include any $v_{\text{eff}} < 0.1$ as this was the effective variance assumed for each grid box of the model simulations. In contrast to the results from Fig. 5d, Volkmer et al. (2024b) found rather an overestimation in the effective variance. This might be explained by the idealized model that was used for this study, which includes typical measurement uncertainties with respect to the measured value of Q, and hence only indirectly includes errors that might occur for example due to cloud movements or uncertainties in the cloud top height.

Figure 6 illustrates the sensitivity of the single mode fit on both the effective radius and variance of the input. In panel **(a)**, the mean bias of the retrieved effective radius is shown with red values denoting an overestimation while blue regions show

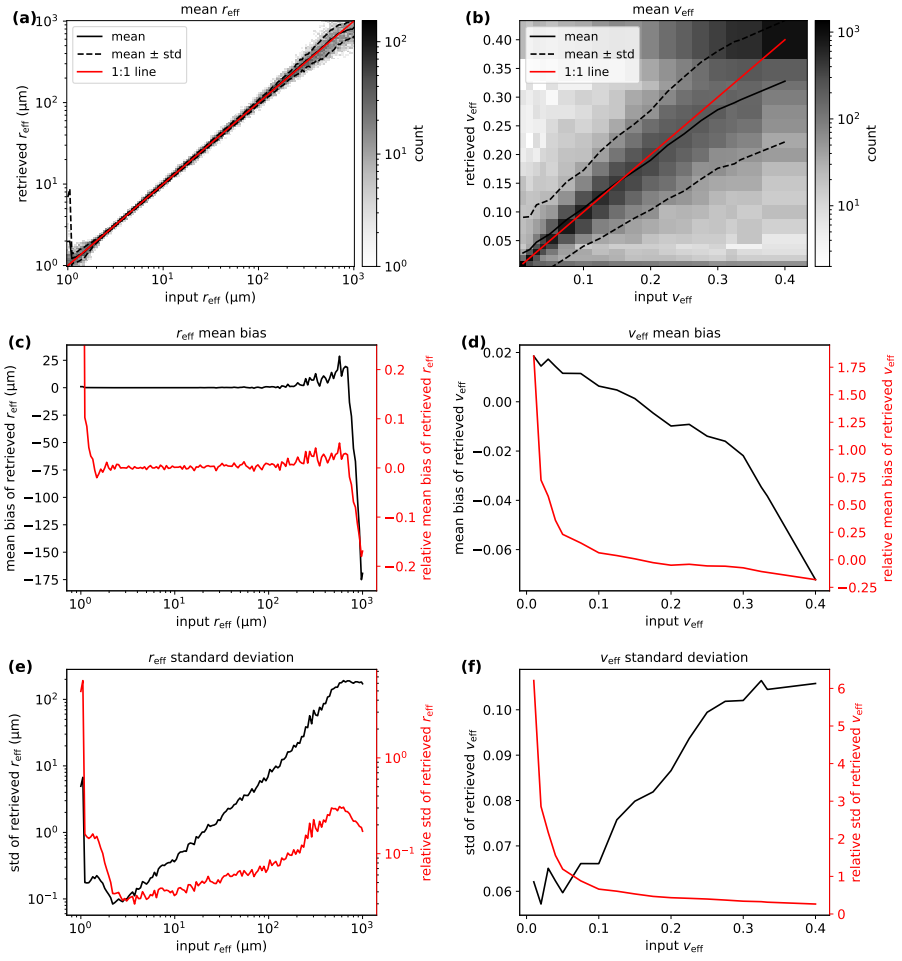


Figure 5. Sensitivity of the single mode fit with respect to the effective radius and the effective variance. In **(a)**, the derived effective radius is plotted with respect to the actual input radius. The black line shows the mean radius derived for each input radius, while the two black dashed lines are the mean plus/minus the standard deviation of each interval. The red line denotes the 1:1 line. The same is shown for the effective variance in panel **(b)**. In **(c)** and **(d)**, the absolute mean bias is shown in black for each effective radius and variance respectively. In red, the relative mean biases are depicted. The same is shown for the standard deviation (black) and relative standard deviation (red) for the effective radius **(e)** and variance **(f)**.

underestimates. Each pair of input $(r_{\text{eff}}, v_{\text{eff}})$ was calculated 12 times. As expected, larger uncertainties are found for larger input r_{eff} with both overestimates and underestimates occurring. However, overestimates tend to dominate in the beginning while underestimates take over the larger the effective radius, which might be due to the end of the LUT coming closer as discussed before. This shift from over- to underestimates tends to occur later for smaller effective variances, while the effective radii are mostly underestimated for the smallest effective variance of 0.01. Finally, the overestimation of the effective radius for small effective radii as seen already in Fig. 5a is also visible, with the largest overestimates occurring for small effective

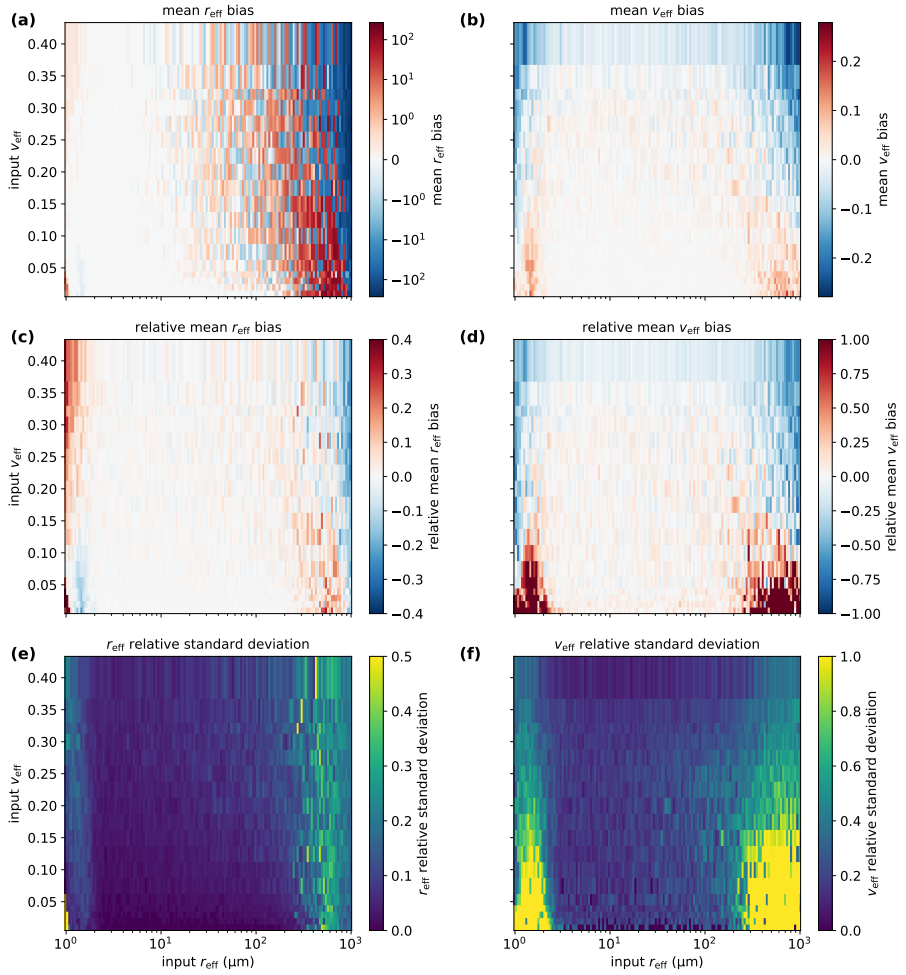


Figure 6. Sensitivity of the single mode fit with respect to the effective radius and the effective variance. In **(a)**, the mean bias of the effective radius is plotted with respect to the input effective radius and variance. Overestimates are shown in red, while underestimates are shown in blue. The mean bias of the effective variance is depicted in panel **(b)**. In **(c)** and **(d)**, the relative mean bias is shown for the effective radius and variance respectively. Panel **(e)** and **(f)** illustrate the relative standard deviations.

variances. Further slight overestimates can be seen for larger variances, while there is hardly any overestimation for medium effective variances between about 0.07 and 0.16. Fig. 5c shows the relative mean bias for each pair of $(r_{\mathrm{eff}}, v_{\mathrm{eff}})$. As before, it is mostly well below $10\,\%$, particularly for $2\,\mu\mathrm{m} \lesssim r_{\mathrm{eff}} \lesssim 200\,\mu\mathrm{m}$ and $v_{\mathrm{eff}} \lesssim 0.1$. The corresponding relative standard deviation is shown in panel **(e)**. As stated above, most of the values are well below 0.5 except for very small effective radii smaller than $2\,\mu\mathrm{m}$ and low effective variances as well as single outliers at larger effective radii ($\gtrsim 200\,\mu\mathrm{m}$).

The analog plots for the effective variance are shown in panel **(b)**, **(d)** and **(f)**. While large effective variances tend to be underestimated especially at very small effective radii ($\lesssim 2\,\mu\mathrm{m}$) and for large effective radii $\gtrsim 200\,\mu\mathrm{m}$, the opposite holds for

small effective variances $\lesssim 0.1$. Parts of this might be explained by the end of the LUT, although the determination of the effective variance works well in between except for slight overestimates for $0.15 \lesssim v_{\text{eff}} \lesssim 0.25$. This is reflected by the relative mean bias in panel **(d)**, with overestimates above $100\,\%$ occurring only for $v_{\text{eff}} < 0.1$ and $r_{\text{eff}} < 3\,\mu\text{m}$ or $r_{\text{eff}} > 200\,\mu\text{m}$. In between, slightly red colors seem to dominate except for $v_{\text{eff}} \gtrsim 0.27$. This might explain the findings of Volkmer et al. (2024b), that the effective variance is overestimated while we found on average rather underestimates for $v_{\text{eff}} \gtrsim 0.12$ from Fig. 5d, which seems to be dominated by the underestimates at very small and very large effective radii. The relative standard deviation in panel **(f)** shows a similar picture with large values occurring particularly at small and large effective radii. Hereby, values larger than 1 are found at small effective variances smaller than about 0.15 and for $r_{\text{eff}} \lesssim 3\,\mu\text{m}$ and $r_{\text{eff}} \gtrsim 200\,\mu\text{m}$. Hence, for those ranges the determination of the effective variance becomes highly uncertain, which is as expected from Fig. 2.

In conclusion, an accurate determination of the effective radius is still possible even for larger effective radii where the phase functions become less distinct, in particular with respect to the relative mean bias and standard deviation. For the effective variance larger uncertainties were found towards larger effective radii, and particularly small effective variances might be hard to determine.

3 Results

In the following section, we show a measurement example of a precipitating cumulus congestus observed on 07-09-2024 around 13:50 UTC with one of the polarization cameras of specMACS in the vicinity of Barbados during the PERCUSION campaign. Figure 7a shows the measured RGB image and Fig. 7b the degree of linear polarization (DOLP) as an RGB composite of the three color channels of the camera. Both panels contain a zoom into the region where the rainbow can be seen. While it is not easy to see in the normal RGB image, it becomes clearly visible in the RGB DOLP composite due to the shift of the minimum of the (polarized) phase function between the individual color channels and the much weaker background signal.

Further evidence of rain within the observed cloud is found in the data of the $35.5\,\text{GHz}$ cloud radar of the HAMP microwave package (Mech et al.; Ewald et al., 2019), which was operated simultaneously to specMACS on board of HALO as part of the "cloud observatory" payload (Stevens et al., 2019; Konow et al., 2021). Figure 8 shows the maximum radar reflectivity projected to the specMACS polarization RGB image in panel **(a)** and the corresponding vertical cross section of the measured radar reflectivity in panel **(b)**. The measurements with the large reflectivities show clearly hydrometeors reaching the ground, and hence indicate the presence of rain. Of course it should be mentioned again, that specMACS does not penetrate through the cloud, but the sideward viewing geometry allows the observation of rain close to the cloud edges and in case of advection.

Figure 9 shows the (unfiltered) polarimetric single mode retrieval results. The interpolated cloud top height derived by the stereographic retrieval (Kölling et al., 2019; Volkmer et al., 2024a) depicted in panel **(b)** indicates cloud tops up to about $6000\,\text{m}$. The derived effective radius (panel **c**) and effective variance (panel **d**) are only available for a limited area which is the region of cloud targets which were observed under the required range of scattering angles between 135° and 165° such that the polarimetric single mode retrieval can be applied. The effective radius shows smaller values for lower cloud top heights, while the observed radii become generally larger at higher altitudes. Next to the region where the rainbow is observed, a clear

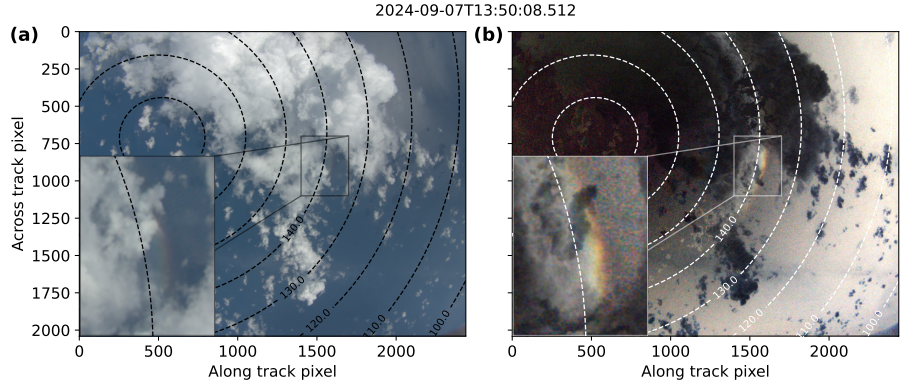


Figure 7. Measurement example of a raining cumulus cloud observed on 07-09-2024 around 13:50:08 UTC by the polarization camera of specMACS. In **(a)**, the RGB image is shown. In **(b)**, the RGB composite of the measured degree of linear polarization (DOLP) of the camera's three color channels can be seen. In the lower left of each subplot a zoom into the region where the rainbow can be seen is shown. The dashed lines denote the scattering angles of the observations.

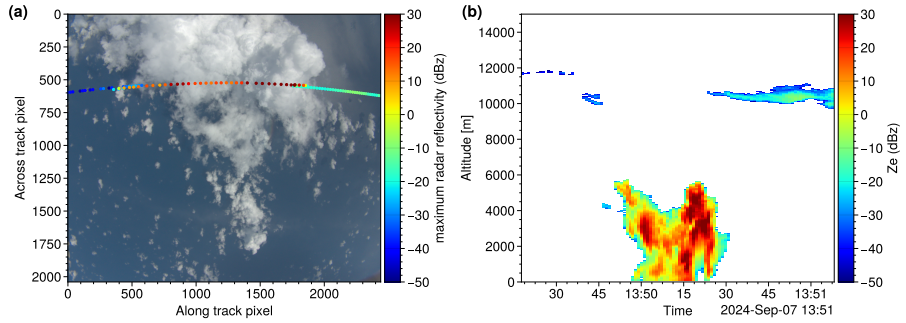


Figure 8. Measurements of the HAMP MIRA cloud radar of the raining cumulus cloud observed on 07-09-2024 around 13:50:08 UTC. In panel **(a)**, the maximum radar reflectivity is shown for each point in time projected to the RGB image of the polarization camera of specMACS. In panel **(b)**, the vertical cross-section of the radar reflectivity can be seen.

signal of large effective radii at the end of the LUT (around $40\,\mu\mathrm{m}$) can be seen. This may already indicate that the single-mode retrieval, and particularly its LUT, is not sufficient in this case. In panel **(e)** and **(f)** the quality measures of the single mode fit, namely the RMSE (Eq. (22)) and QI (Eq. (23)) respectively, are shown. Values that are outside the valid range for the single mode retrieval (RMSE > 2.5 and QI < 4) are marked in black. It can be seen that the region of larger effective radii close to the observed rainbow shows higher RMSE (although not all of the points fall outside the valid range) and in particular smaller QI values outside the valid range. This further indicates that the single mode fit does not sufficiently explain the observed polarized signal.

Those points are input to the multimode retrieval and Fig. 10 shows the results of the individual modes of the cloud targets. The points shown were filtered by the same thresholds as for the single mode retrieval: Points with RMSE > 2.5 and QI < 4

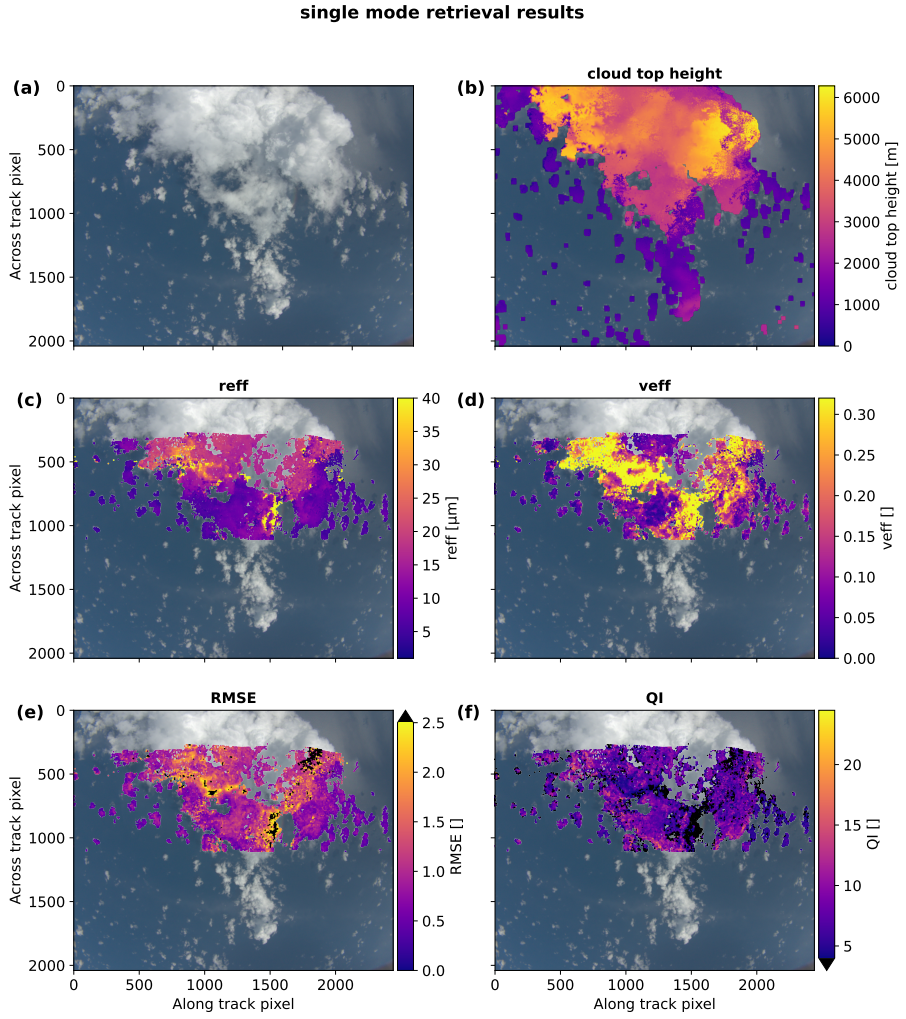


Figure 9. Results of the polarimetric single mode cloudbow retrieval for the measurement example of the raining cumulus cloud observed on 07-09-2024 around 13:50:08 UTC by the polarization camera of specMACS. Panel **(a)** shows the RGB image taken by the camera, while the cloud top height is projected to the image in panel **(b)**. In **(c)** and **(d)**, the derived effective radius and respectively variance can be seen. In **(e)** and **(f)**, the RMSE and quality index of the single mode fit are shown. Targets with RMSE > 2.5 and QI < 4 are marked in black in the respective panel.

395 were filtered out to ensure the quality of the results. In Fig. 10a-c, the resulting effective radii are shown for the three modes, while panel **(d)**-**(f)** show the corresponding effective variances. Panels **(g)**-**(i)** show the signal fraction f_A as defined in Eq.(13), whereas panels **(j)**-**(l)** depict the corresponding droplet number concentration fraction f_N after Eq.(19). From Fig. 10a and 10b, we can see that the resulting effective radius for the two dominant modes occurs in patches of smaller and larger values and not randomly, which is a good initial indication of the credibility of the results. Most of the r_{eff} values of the dominant mode

(Fig. 10a) are between about $10\,\mu\mathrm{m}$ and $100\,\mu\mathrm{m}$, same for the second mode (Fig. 10b). Figure 10c shows on the other hand that there are mainly two regions that need a third mode for an accurate explanation of the signal: close to the observed rainbow and further towards the upper right of the image. Hereby, the resulting r_{eff} seem to be less structured, however, as pointed out in Fig. 10i, most of them contribute only with a few percent to the measured signal. Comparing Fig. 10a and Fig. 10b in more detail, it can be seen that the derived effective radii are to some extent complementary in a manner that when a larger r_{eff} ($\mathcal{O}(100\,\mu\mathrm{m})$) is retrieved as the first mode, then a smaller r_{eff} ($\mathcal{O}(10\,\mu\mathrm{m})$) is derived as the second mode and vice versa.

In contrast to the effective radius, the effective variance in Fig. 10d - Fig. 10f shows less structure, although not being completely random as well. This is expected, as it is in general harder to retrieve the effective variance correctly as shown in Fig. 5 and Fig. 6 and e.g. by Alexandrov et al. (2012a); Volkmer et al. (2024b).

Finally, comparing the signal fraction f_A in Fig. 10g-10i to the droplet number concentration fraction f_N in Fig. 10j-10l shows clearly that f_N is dominant for smaller effective radii independent of f_A. This is due to the proportionality of f_N to $1/r_{\text{eff}}^2$ as shown in Eq.(19).

In Fig. 11, the resulting RMSE and QI of the multimode fit is shown for all points that were input to the multimode retrieval. Points that are filtered due to increased RMSE > 2.5 or low QI < 4 values are shown in black. While only a few black points occur in the RMSE plot, most points filtered are due to a low quality index as indicated by the black points in panel **(b)**. In total, we find for the example given here (so all points that are within the specMACS image shown) 2590 input targets to the multimode retrieval of which $62.5\,\%$ are valid. For the other targets, the signal is still not well explained even with several modes. A reason for this might be other uncertainties in the aggregation of the measured signal, e.g. due to the development of the cloud, convective movement, which is not captured in the mean wind from ERA5 data used in the single mode retrieval (Pörtge et al., 2023), or potential uncertainties in the cloud top height, which are needed for the correct identification of cloud targets in subsequent images. Further, $71.4\,\%$ of the valid targets have a RMSE less than 1.2, which is the threshold for adding a new mode. Together with the single mode retrieval, the example shown consists of 19246 cloud targets of which $80.4\,\%$ are valid with respect to the filters applied to the single mode retrieval results. Hence, with the multimode retrieval, we increase the number of valid targets to $88.8\,\%$. Even though this corresponds just to an increase of about $8.4\,\%$, we obtain valuable information about cloud microphysics, i.e. where multiple modes exist in the DSD and under which conditions they coexist. The improvement in the RMSE of the valid targets in the example compared to the RMSE of the single mode retrieval is on average $47.6\,\%$, while we find an average increase of the QI of $145.0\,\%$.

A remaining question to consider is whether large droplets can really be seen at the higher cloud tops as indicated by Fig. 10 and Fig. 9b. To this end, Fig. 12 combines the cloud targets from specMACS within the 1° cone around the radar beam with the radar measurements and optical thickness measurements of the WAter vapor Lidar Experiment in Space (WALES; Wirth et al., 2009; Wirth and Groß, 2025). In panel **(a)** we show the radar reflectivity as in Fig. 8b, but this time overlayed with the cloud top heights (mean, minimum, and maximum) of the retrieved targets within the cone. The heights of the specMACS cloud targets are partly well below the radar heights (excluding the cirrus above), i.e. towards the upper left of the deeper convective cloud, which indicates that specMACS is sensitive to targets deeper within the cloud. The optical thickness at $532\,\mathrm{nm}$ measured by WALES is shown in panel **(b)** together with the corresponding cloud target heights, illustrating that the mean height of the

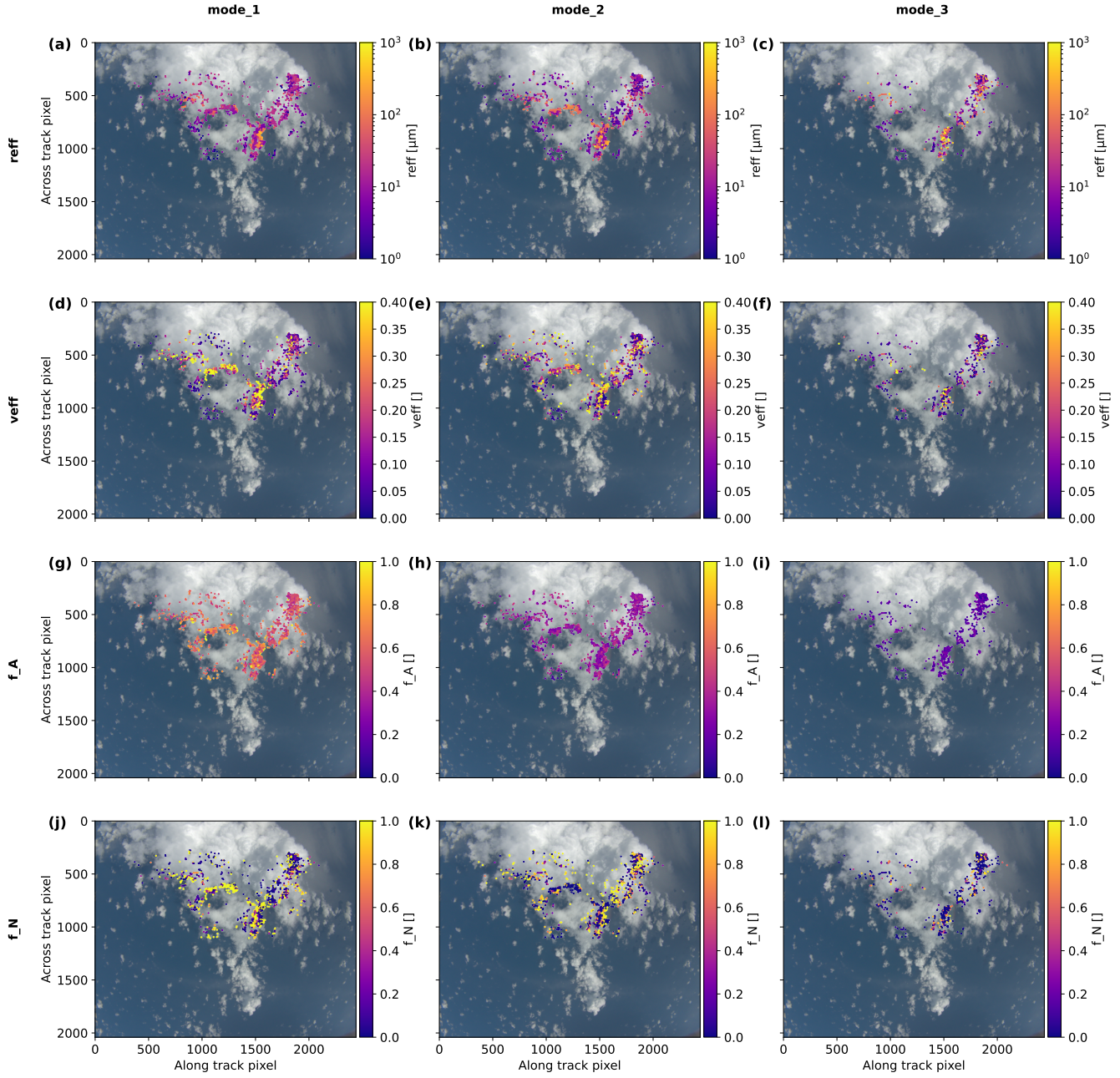


Figure 10. Results of the multimode approach for the measurement example of the raining cumulus cloud observed on 07-09-2024 around 13:50:08 UTC by the polarization camera of specMACS. The columns of the figure depict the individual modes, while the rows show the derived effective radius (panel **a**, **b** and **c**), the effective variance (panel **d**, **e** and **f**), the signal fraction f_A (panel **g**, **h** and **i**) and the droplet number concentration fraction f_N (panel **j**, **k** and **l**).

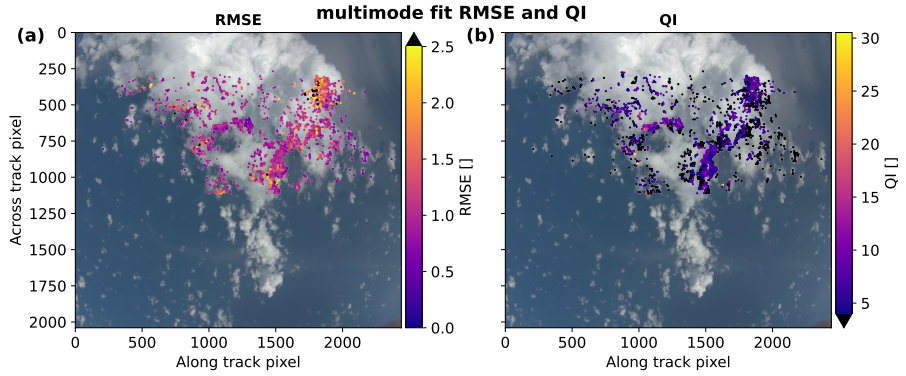


Figure 11. Quality measures of the multimodal fit results. In panel **(a)**, the RMSE calculated after Eq. (22) of all points is projected to the RGB image of the polarization camera of specMACS. In **(b)**, the corresponding plot is shown for the QI of the multimode fit calculated after Eq. (24). As for the single mode retrieval, points with RMSE > 2.5 or respectively QI < 4 are shown in black and mark the points which are filtered from the results of the multimode fit.

retrieval points from specMACS is well in line with the attenuation of the lidar at optical thicknesses around one. Thus, this might be evidence that specMACS penetrates into the areas where the radar shows an enhanced reflectivity and large droplets might be present as the optical thickness above is low. In panel **(c)**, we show the corresponding effective radii derived for the up to three modes. The dominant mode depicted in red shows targets with values up to about $100\,\mu\mathrm{m}$ around 13:50 UTC, exactly where the mean of the specMACS cloud target heights coincides with the higher radar reflectivity.

While the example shown gives an indication for the capability of the multimode fit retrieval to derive the individual parameters of the CDSD of cloud targets consisting of a superposition of multiple gamma distributions, a more qualitative comparison of the resulting fit of individual targets to the measured signal, the original result of the single mode fit and the Rainbow Fourier Transform (RFT, Alexandrov et al., 2012b) will be given in the next section.

3.1 Evaluation of single targets and comparison to RFT

As shown in the previous section, the effective radius of the multimode retrieval shows some systematic patterns for the derived modes, which hints towards a stable retrieval algorithm. To further evaluate the results, we compare the results for four individual targets in Fig. 13 - Fig. 16 to the original result of the single mode fit and the RFT. All four figures show the location of the target in panel **(a)**, and the measured signal, the resulting multimode fit as well as the single mode fit result and RFT fit result in panel **(b)**. The RFT fit result is computed from the result of the mode decomposition after Alexandrov et al. (2015) as

$$Q_{\mathrm{fit,RFT}} = A_{\mathrm{RFT}} \sum_{i=1}^{M} \zeta_i \cdot P_{12}^{i}[r_{\mathrm{eff},i}, v_{\mathrm{eff},i}](\theta) + B_{\mathrm{RFT}} \cdot \cos^2(\theta) + C_{\mathrm{RTF}}, \tag{25}$$

where ζ_i is the percentage scale of each mode derived from the mode decomposition and the parameters A_{RFT}, B_{RFT} and C_{RFT} are derived from a least-squares fit to the measurements, which makes the results of the RFT and the multimode retrieval

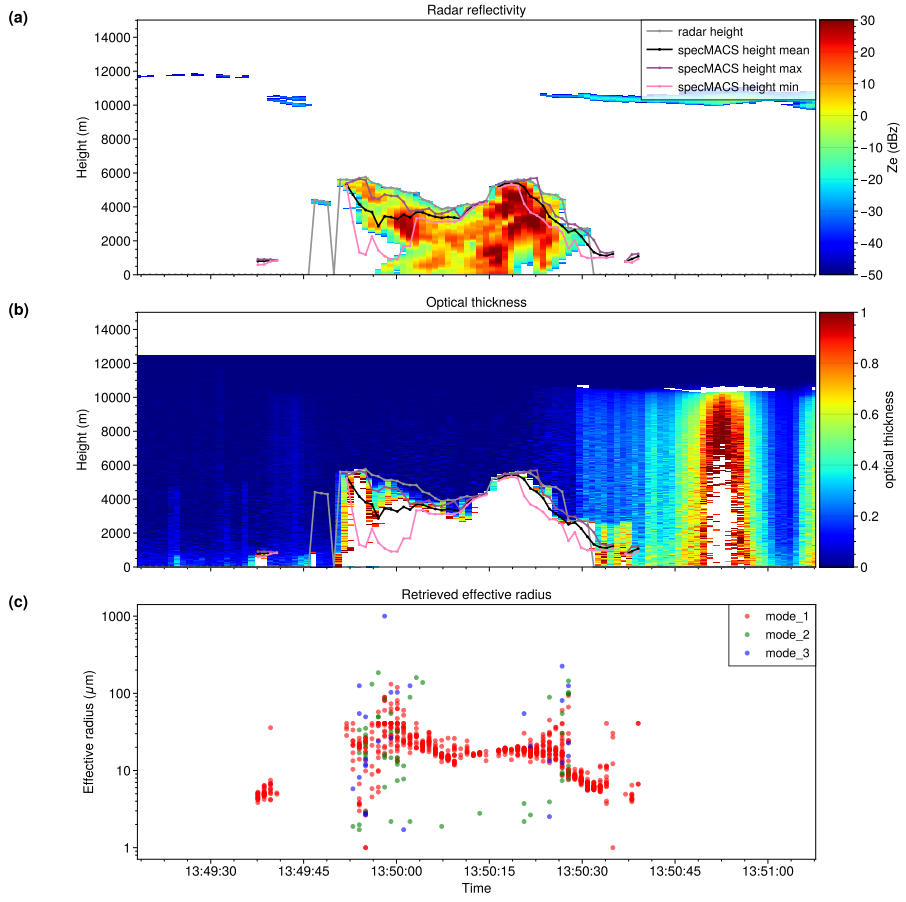


Figure 12. Timeline of the retrieval results within the 1° cone around the radar beam related to the radar reflectivity (panel **(a)**), and the optical thickness derived from lidar measurements (panel **(b)**). The retrieval results are shown for the individual modes in panel **(c)**. In **(a)** and **(b)**, the cloud top height of the radar (without cirrus) is shown in grey, together with the mean (black), the maximum (purple) and the minimum (pink) cloud top height of the specMACS cloud targets within the cone.

comparable as best as possible. Panel **(c)** and **(d)** show the resulting so-called area size distributions of the single mode, and the multimode fit results as well as the distributions derived by the RFT and the corresponding mode decomposition. The area size distribution is hereby defined by Alexandrov et al. (2012b) as

$$n_a(r) = \frac{r^2 n(r)}{\int_0^\infty r^2 n(r) dr}, \tag{26}$$

where $n(r)$ is the droplet size distribution as in Eq.(6). As the area distribution defines another gamma distribution which can be described in the same form as in Eq.(6), the "effective radius" and "effective variance" of the area distribution $r_{\text{eff},a}$ and

respectively $v_{\text{eff},a}$ can be derived from the effective radius and variance of the droplet size distribution as

$$r_{\text{eff},a} = r_{\text{eff}}(1 + 2v_{\text{eff}}) \text{ and } v_{\text{eff},a} = \frac{v_{\text{eff}}}{1 + 2v_{\text{eff}}}. \tag{27}$$

The corresponding inverse transformation is given by

$$r_{\text{eff}} = r_{\text{eff},a}(1 - 2v_{\text{eff},a}) \text{ and } v_{\text{eff}} = \frac{v_{\text{eff},a}}{1 - 2v_{\text{eff},a}}, \tag{28}$$

allowing to calculate the one distribution from the parameters of the other. Panel **(c)** and **(d)** differ from each other as we used a logarithmic scale in panel **(d)** to eventually show the multimodal structure more clearly, as larger cloud droplets are suspect to much lower cloud droplet number concentrations.

In Fig. 13, the measured polarized radiance (panel **b**) and the results from the multimode fit (red), the RFT (blue) and the single mode fit (green) are shown for a cloud target located within the region close to the observed rainbow, where at least two modes were found in the shown figures in Sec. 3. This example shows a double cloudbow as obtained from the combination of phase functions shown in Fig. 3. Furthermore, we can observe two supernumerary minima, which hints to at least one mode with a narrow DSD, which is also what we find both from the multimode fit and the RFT: The multimode fit sees two modes, a signal dominating one with $r_{\text{eff},1} = 185\,\mu\text{m}$ and a second one with $r_{\text{eff},2} = 7.39\,\mu\text{m}$. While the first mode is broad ($v_{\text{eff},1} = 0.4$), the small droplet mode has a narrow distribution with $v_{\text{eff},2} = 0.01$ explaining the supernumerary bows. From panel **(b)**, it can be seen that the found combination explains the measured signal very well with a RMSE of 1.17. The mode decomposition of the RFT on the other hand, finds a first mode that is with $r_{\text{eff},1} = 7.65\,\mu\text{m}$ and $v_{\text{eff},1} = 0.03$ very similar to the small droplet mode found from the multimode fit. It further finds a second mode with even smaller droplets and $r_{\text{eff},2} = 4.22\,\mu\text{m}$ and $v_{\text{eff},2} = 0.05$. Panel **(c)** hereby reveals, that both retrieval results find a distribution with a narrow peak around $7\,\mu\text{m}$, where both distributions are well aligned. In contrast, the multimode retrieval does not retrieve the secondary peak towards the left of the main peak of the RFT distribution, while panel **(d)** shows that the underlying broader distribution with its maximum around $150\,\mu\text{m}$ is missed by the RFT. This is due to the fact that the RFT in its current implementation only retrieves radii up to $100\,\mu\text{m}$ in the area size distribution, which means that the effective radii retrieved from the mode decomposition are in general lower than $100\,\mu\text{m}$. Moreover, the mode decomposition technique finds peaks in the area size distribution, but since droplet number concentrations are usually much smaller for larger droplets as can be seen from the distribution retrieved from the multimode retrieval in **(c)**, peaks at larger droplets might also be missed in general by the method. From panels **(c)** and **(d)**, we can also see one issue, that we usually observe when applying the RFT to specMACS measurements: the derived area size distribution shows negative values which are not removed by the corrections described by (Alexandrov et al., 2012b) making the results at least partly physically unrealistic.

The results of the cloud target in Fig. 14 also show a clear multimodal structure as the target in Fig. 13. In panel **(b)**, we can clearly see that the signal is well explained by the new multimodal fit (red), while the single mode fit does not capture the measured signal properly. Here, the multimode fit finds two modes with $r_{\text{eff},1} = 152\,\mu\text{m}$ and $r_{\text{eff},2} = 7.76\,\mu\text{m}$. Again, the first mode is broad with an effective variance of $v_{\text{eff},1} = 0.4$, while this time, also a broader distribution of the second mode is found with $v_{\text{eff},2} = 0.25$. From the single mode retrieval, a radius of $r_{\text{eff,max}} = 40.77\,\mu\text{m}$ is found, which is consistent with the

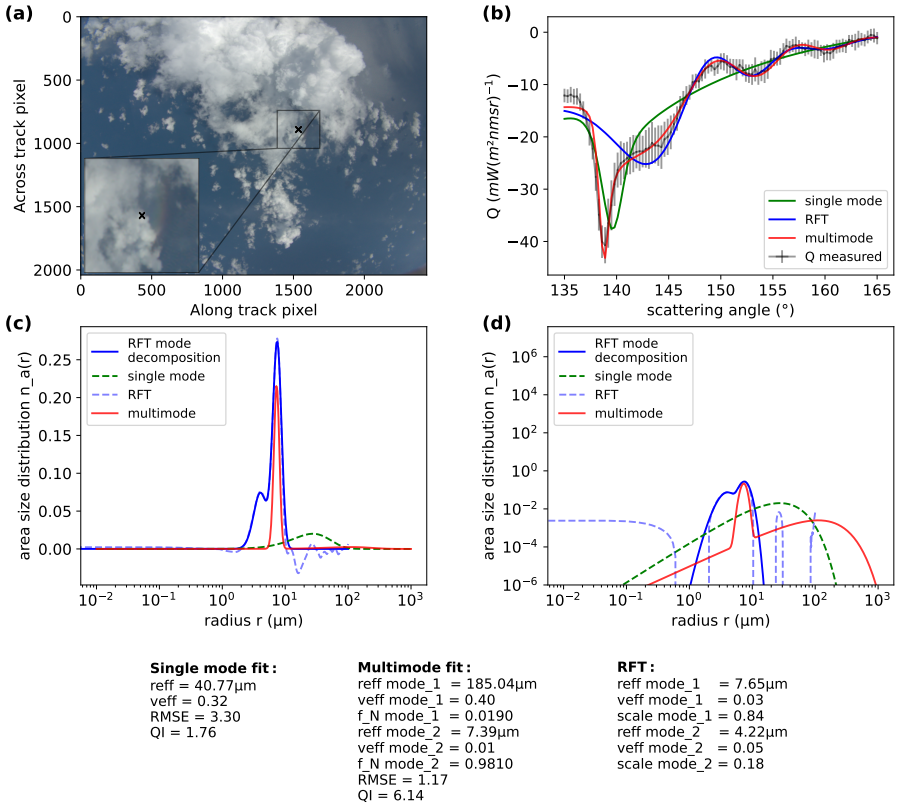


Figure 13. Retrieval results for an individual cloud target. The location of the target with respect to the image taken by the specMACS polarization camera taken around 13:50:08 UTC on 07-09-2024 is shown in panel **(a)**. In **(b)**, the measured Q component of the stokes vector is shown (grey with errorbars), the resulting fit of the multimode retrieval (red) as well as the original single mode fit (yellow) and the RFT mode decomposition result (blue) is shown. In panel **(c)** and **(d)**, the coresponding area distributions derived from the retrievals are shown without and with a logarithmic scale of the y-axis.

maximum radius of the LUT. The RFT finds four modes from the mode decomposition with effective radii $r_{\text{eff},1} = 4.12\,\mu\text{m}$, $r_{\text{eff},2} = 6.63\,\mu\text{m}$, $r_{\text{eff},3} = 12.15\,\mu\text{m}$ and $r_{\text{eff},4} = 8.47\,\mu\text{m}$. This results in a fit calculated after Eq.(25) that seems to capture the lower effective radius mode well, while it does not explain the signal originating from the large droplets. Here, panel **(d)** makes clear that the RFT misses droplets larger than $100\,\mu\text{m}$ where currently the definition of the RFT ends.

The example shown in Fig. 15 shows the capability of the multimode retrieval to explain the measured signal with three modes: One with $r_{\text{eff},1} = 14.64\,\mu\text{m}$ and an effective variance of 0.30, a second one with an effective radius of $60.24\,\mu\text{m}$ and an effective variance of 0.4 and one with $r_{\text{eff},3} = 5.00\,\mu\text{m}$ and $v_{\text{eff},3} = 0.1$. Altogether, the measured signal is described with a RMSE of 0.51 and a high quality index of 23.29 is found. In comparison, the mode decomposition from the RFT finds

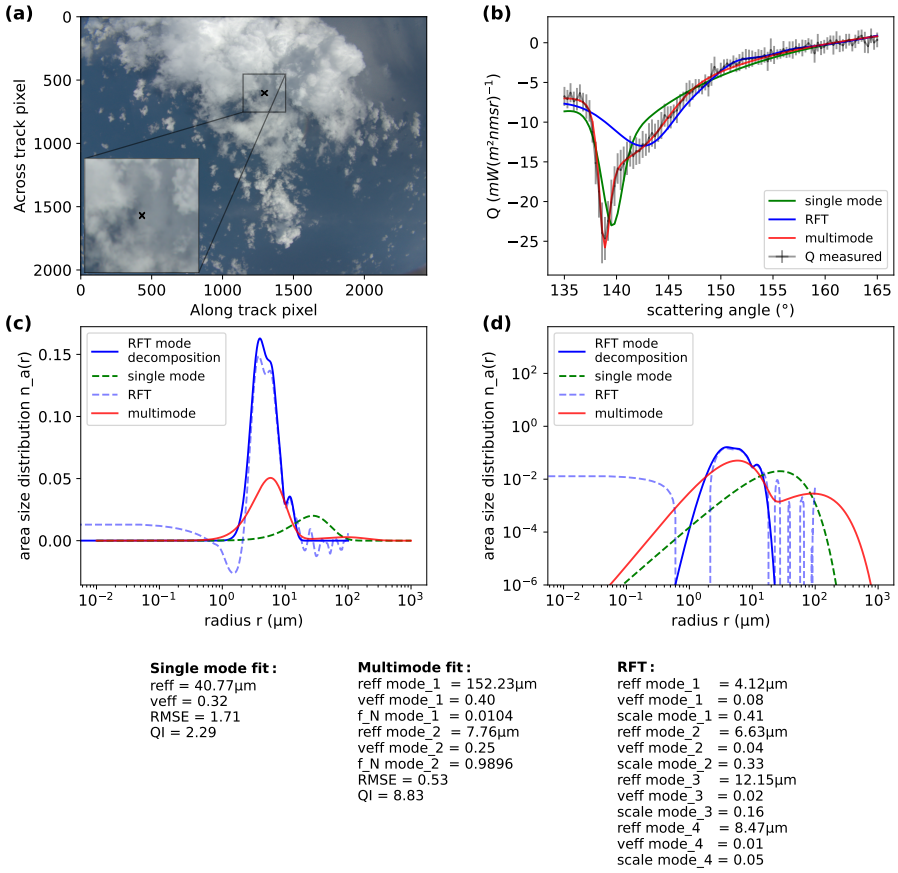


Figure 14. Same as in Fig. 13 but for another cloud target.

two modes, a first mode with $r_{\text{eff},1} = 5.36\,\mu\text{m}$ and $v_{\text{eff},1} = 0.18$, which is on the same order of the third mode found by the multimode and a second mode with $r_{\text{eff},2} = 16.87\,\mu\text{m}$ and $v_{\text{eff},2} = 0.09$. The resulting DSDs in panel **(c)** and **(d)** show that the DSDs of the RFT and the multimode retrieval are very similar. The major peak around $5\,\mu\text{m}$ is both found by the RFT and the multimode retrieval and both distributions show a tail towards larger droplets, although the small peak around $11\,\mu\text{m}$ is not as pronounced in the multimode retrieval as in the RFT. As before, the signal computed by the mode decomposition result does not describe the actual measured signal completely, which is most likely due to the missing contribution from the mode around $60\,\mu\text{m}$. This mode derived by the multimode retrieval is not encountered by the mode decomposition of the RFT, since droplet numbers are too small compared to the smaller droplets. In this example, the single mode fit does not hit the maximum effective radius of the LUT, but finds an effective radius of $15.16\,\mu\text{m}$. This corresponds to a combined effective radius which lies in between the $14.64\,\mu\text{m}$ found by the multimode retrieval and the $16.87\,\mu\text{m}$ of the RFT.

Figure 16 shows an example target, where the RFT captures the supernumerary bows of the measured signal very well, while the multimode retrieval fits the main minimum and the second minimum but not the supernumerary bows. Hereby, the

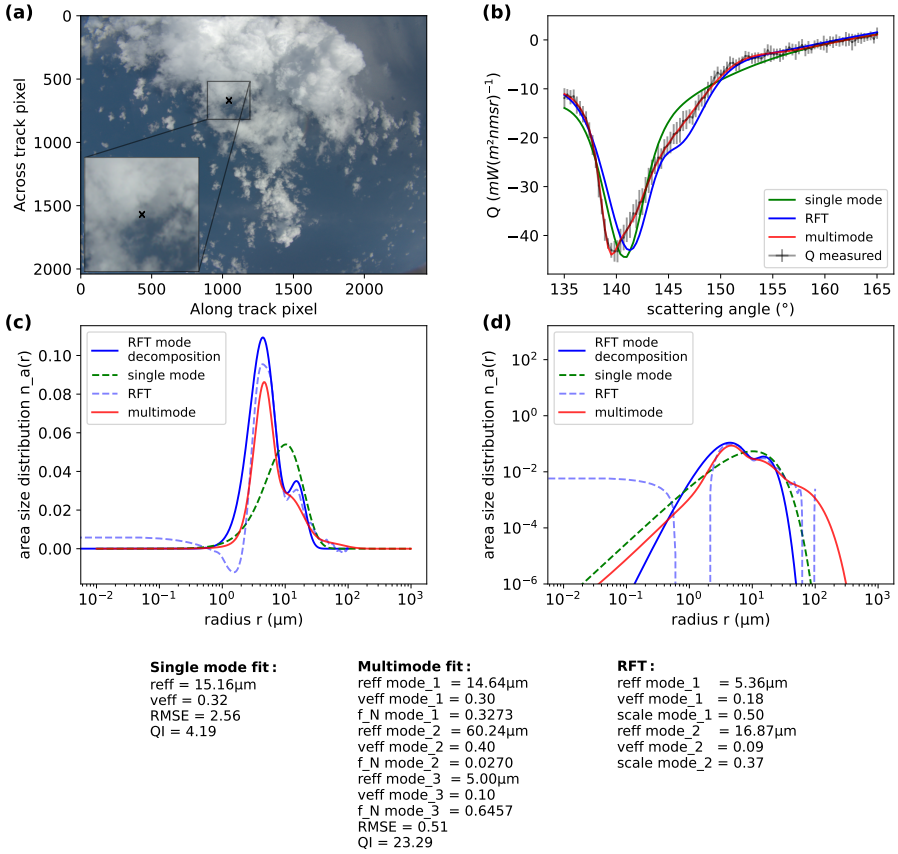


Figure 15. Same as in Fig. 13 but for another cloud target.

mode decomposition of the RFT finds three modes, each with a rather small distribution: A first mode with $r_{\text{eff},1} = 4.75\,\mu\text{m}$ and $v_{\text{eff},1} = 0.06$, a second one with $r_{\text{eff},2} = 16.77\,\mu\text{m}$ and $v_{\text{eff},2} = 0.02$, and a third one with $r_{\text{eff},3} = 7.81\,\mu\text{m}$ and $v_{\text{eff},3} = 0.02$ are found. This explains that the supernumerary bows are fitted well by the RFT, while on the other hand, the multimode fit finds three modes as well with $r_{\text{eff},1} = 84.77\,\mu\text{m}$ and $v_{\text{eff},1} = 0.08$, a second one with $r_{\text{eff},2} = 15.37\,\mu\text{m}$ and $v_{\text{eff},2} = 0.15$, and a third one with $r_{\text{eff},3} = 4.12\,\mu\text{m}$ and $v_{\text{eff},3} = 0.23$. While the effective radii of both second modes are similar, the effective variance of the multimode fit is larger. This holds in general for all three modes and might explain why the multimode fit does not capture the supernumerary bows. Again, the RFT mode decomposition is subject to smaller effective radii and does not find the larger mode with an effective radius of about $84\,\mu\text{m}$, which explains why the fit does not capture the major minimum. Furthermore, the single mode retrieval is again biased towards larger radii and finds the maximum effective radius of the LUT with $r_{\text{eff,max}} = 40.77\,\mu\text{m}$ and a broad distribution ($v_{\text{eff}} = 0.32$). Panel **(c)** and **(d)** show, that the resulting size distributions differ between the different methods, although both the multimode distribution and the distribution from the RFT show three maxima,

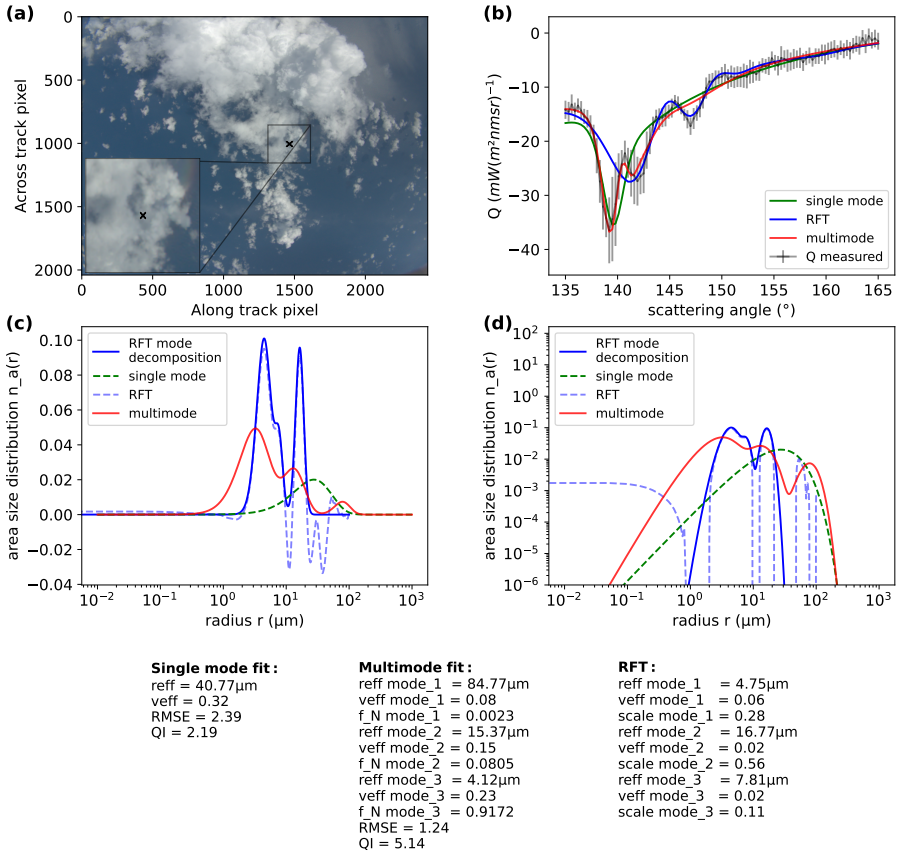


Figure 16. Same as in Fig. 13 but for another cloud target.

but they are shifted. One explanation for the deviation of the methods might be the noise of the measured data in panel **(b)**, which could be related to errors in the tracking of the target and hence, errors in the retrievals.

4 Discussion and Conclusion

In this work, we presented a new technique that builds on existing retrievals of cloud droplet size distributions using polarized measurements of the cloudbow, but takes more than one mode into account. The existing polarimetric CDSD retrievals are constrained to single mode gamma distributions with maximum effective radii of about $40\,\mu m$ used by Pörtge et al. (2023) for the specMACS measurements. For POLDER, Shang et al. (2019) use a LUT with effective radii between $3\,\mu m$ and $25\,\mu m$, while Alexandrov et al. (2015) use a table with effective radii between $5\,\mu m$ and $30\,\mu m$ for the RSP retrieval, and the LUT for the evaluation of the AirHARP measurements includes effective radii ranging between $5\,\mu m$ and $20\,\mu m$ (McBride et al., 2020) . We extended the existing LUT used by Pörtge et al. (2023) to an effective radius of $1000\,\mu m$ and showed, based on

a measurement example from the PERCUSION campaign, that this is necessary to be able to describe the measured signal in deep convective clouds. It was shown that despite the increasing similarity of the polarized phase functions towards higher effective radii, an estimate of the effective radius is still possible with a relative mean absolute bias of less than $10\,\%$ for a broad range of effective radii between about $1.5\,\mu\mathrm{m}$ and $800\,\mu\mathrm{m}$ (compare Fig. 5c) considering the measurement uncertainty of the specMACS cameras. This is the required relative accuracy to measure aerosol and cloud forcings in climate change from space according to Mishchenko et al. (2004). The standard deviation increases for larger radii with a maximum occurring around $500\,\mu\mathrm{m}$ of about $30\,\%$. Only $r_{\mathrm{eff}} \lesssim 1.5\,\mu\mathrm{m}$ show even larger standard deviations. In terms of the effective variance, an increase in the mean bias and standard deviation towards small effective variances was found, particularly at very small ($< 3\,\mu\mathrm{m}$) and large effective radii $\gtrsim 200\,\mu\mathrm{m}$. Nonetheless, the absolute mean bias of v_{eff} was found to be less than $50\,\%$ for $v_{\mathrm{eff}} \gtrsim 0.03$. We assumed a simple model for the measurement uncertainty which describes the variability in Q in dependence of Q itself. Hence, possible uncertainties in the signal aggregation process, e.g. due to wrong cloud top height estimates, convective cloud movements which are not described by the mean wind field estimate of the ERA5 data (Hersbach et al., 2020), or other biases in the aggregated signal in real measurements, such as shadows within the target region or ocean signals, were not taken into account. Studying how the existence of multiple modes affects the accuracy of the cloud droplet size distribution retrieval is subject to further studies.

Further uncertainties in the retrieval of larger effective radii might also be introduced by the implicit assumption of spherical droplets with the calculation of the scattering phase matrix elements using Mie theory. The shape of water droplets is spherical for radii up to about $400 - 500\,\mu\mathrm{m}$, while they are described by spheroids in the radius range up to about $1\,\mathrm{mm}$ (Sec. 2.1.6 of Pruppacher and Beard, 1970; Beard and Chuang, 1987; Chuang and Beard, 1990). The deviation from spheres further increases for even larger droplets. First studies investigated the influence of the shape of rain droplets on the phase function compared to perfect spheres. For example, Macke and Großklaus (1998) used geometric optics for the phase function calculation of typical rain droplet size distributions and investigated the influence on the backscatter properties for lidar applications. Sadeghi et al. (2012) performed simulations of rainbows for non-spherical particles. However, they considered homogeneous size distributions only. The influence of non-spherical particles on the phase functions used in this work and possible implications on the derivation of size distributions from polarized measurements of the cloudbow will be investigated in the future.

Nonetheless, a conceptual framework of this new approach towards the retrieval of multimodal size distributions was given, and first results indicate the capability of the new fitting strategy based on a real measurement example. It could be seen that close to a rainbow observed in the measurements, a significant amount of targets show results with more than one mode. Moreover, the results included at least one mode with effective radii on the order of $100\,\mu\mathrm{m}$, indicating that the observation included a signal originating from larger droplets as expected from the observation of the rainbow in the RGB image and simultaneous radar measurements. While this does not proof the overall concept of the method, examples of individual targets were shown that revealed that in most cases the measured polarized radiance signal is well explained by the multimode fit with up to three modes. Altogether, the single mode fit and the multimode fit are capable of explaining the measured polarized radiance signal of about $88.8\,\%$ of the cloud targets in the example considered, which is an increase of about $8.4\,\%$ compared

to the single mode fit only. The targets improved by considering multiple modes showed an average decrease in the RMSE of about $48\,\%$ compared to the RMSE of the single mode fit. Further, an average increase in the QI of about $145\,\%$ was found.

Moreover, the results of the multimode fit were compared qualitatively for individual targets to the results of the CDSD independent approach of the Rainbow Fourier Transform described by Alexandrov et al. (2012b). The advantage of the RFT is that it does not need an a priori assumption about the size distribution, which, on the other hand, may lead to non-physical results like negative values. Nevertheless, in most cases the DSDs from the RFT and the multimode fit are similar, i.e. that one or several maxima of the distribution are recognized by both retrievals or that one mode found by one of the retrievals encloses the distribution of the other to some part. An improved agreement could e.g. be achieved by extending the RFT beyond $100\,\mu\mathrm{m}$.

In the future, the uncertainty with respect to multiple modes will be investigated both in terms of 1-D and realistic 3-D simulations. Further, the retrieval will be applied to all measurements of the PERCUSION campaign and evaluated with regard to microphysical processes such as precipitation initiation under different meteorological conditions.

Data availability. The specMACS data used for this work are made avalaible under request. The level 2 data of the MIRA Cloud Radar from the HALO Microwave Package can be accessed via the InterPlanetary File System hash ipfs://bafybeifxtmq5mpn7vwiiwl4vlpoil7rgm2tnhmkeyqsyudleqegxzvwl3a. The data of the WALES lidar for the Barbados period of the PERCUSION campaign were published by Wirth and Groß (2025).

Author contributions. The presented method is based on the idea of BM and a first implementation by LD. LV continued the work and made the retrieval applicable to larger flight segments. Further, LV performed the sensitivity studies and prepared the manuscript. LD and BM helped improving the method and the manuscript.

Competing interests. At least one of the (co-)authors is a member of the editorial board of Atmospheric Measurement Techniques.

Acknowledgements. The authors want to thank the specMACS team, namely Veronika Pörtge, Anna Weber, Tobias Zinner, Anja Stallmach, and Zekican Demiralay for operating the instrument during the PERCUSION campaign and the useful discussions regarding the retrieval development. Further, the authors want to thank the entire team of the PERCUSION campaign for the organization, collaboration and support. Special thanks goes to the DLR flight operations team for planning and executing the HALO flights and to Christian Mallaun, Dominika Pasternak, Martin Zöger and Lisa Eirenschmalz for providing the high time resolution BAHAMAS data necessary for the accurate location of the points on cloud surfaces in 3-D space and the evaluation of the whole flights during the campaign. Finally, we want to thank Mikhail Alexandrov and colleagues at NASA GISS for providing the RFT Code, and Selina Bernlochner and Jonas Gunz for making it applicable to the specMACS measurements. This research has been supported by the Deutsche Forschungsgemeinschaft (DFG, German Research

Foundation) within the Priority Project SPP 1294. We used the Github Copilot, ChatGPT, Google AI Studio and the LMU Faculty of Physics inference service (using the Qwen3.6-35B-A3B model and Mistral Vibe as command line interface) for coding assistance.

References

Alexandrov, M. D., Cairns, B., Emde, C., Ackerman, A. S., and van Diedenhoven, B.: Accuracy assessments of cloud droplet size retrievals from polarized reflectance measurements by the research scanning polarimeter, 125, 92–111, https://doi.org/10.1016/j.rse.2012.07.012, 2012a.

Alexandrov, M. D., Cairns, B., and Mishchenko, M. I.: Rainbow Fourier transform, 113, 2521–2535, https://doi.org/10.1016/j.jqsrt.2012.03.025, 2012b.

Alexandrov, M. D., Cairns, B., Wasilewski, A. P., Ackerman, A. S., McGill, M. J., Yorks, J. E., Hlavka, D. L., Platnick, S. E., Thomas Arnold, G., van Diedenhoven, B., Chowdhary, J., Ottaviani, M., and Knobelspiesse, K. D.: Liquid water cloud properties during the Polarimeter Definition Experiment (PODEX), 169, 20–36, https://doi.org/10.1016/j.rse.2015.07.029, 2015.

Beard, K. V. and Chuang, C.: A New Model for the Equilibrium Shape of Raindrops, 44, 1509–1524, https://doi.org/10.1175/1520-0469(1987)044<1509:anmfte>2.0.co;2, 1987.

Bohren, C. F. and Huffman, D. R.: Absorption and Scattering of Light by Small Particles, Wiley, https://doi.org/10.1002/9783527618156, 1998.

Brenguier, J.-L. and Chaumat, L.: Droplet Spectra Broadening in Cumulus Clouds. Part I: Broadening in Adiabatic Cores, Journal of the Atmospheric Sciences, 58, 628 – 641, https://doi.org/10.1175/1520-0469(2001)058<0628:DSBICC>2.0.CO;2, 2001.

Bréon, F.-M. and Doutriaux-Boucher, M.: A comparison of cloud droplet radii measured from space, 43, 1796–1805, https://doi.org/10.1109/tgrs.2005.852838, 2005.

Bréon, F.-M. and Goloub, P.: Cloud droplet effective radius from spaceborne polarization measurements, 25, 1879–1882, https://doi.org/10.1029/98gl01221, 1998.

Cairns, B., Russell, E. E., and Travis, L. D.: Research Scanning Polarimeter: calibration and ground-based measurements, in: SPIE Proceedings, edited by Goldstein, D. H. and Chenault, D. B., SPIE, https://doi.org/10.1117/12.366329, 1999.

Chandrakar, K. K., Cantrell, W., Chang, K., Ciochetto, D., Niedermeier, D., Ovchinnikov, M., Shaw, R. A., and Yang, F.: Aerosol indirect effect from turbulence-induced broadening of cloud-droplet size distributions, 113, 14 243–14 248, https://doi.org/10.1073/pnas.1612686113, 2016.

Chuang, C. C. and Beard, K. V.: A Numerical Model for the Equilibrium Shape of Electrified Raindrops, 47, 1374–1389, https://doi.org/10.1175/1520-0469(1990)047<1374:anmfte>2.0.co;2, 1990.

Deirmendjian, D.: Scattering and Polarization Properties of Water Clouds and Hazes in the Visible and Infrared, 3, 187, https://doi.org/10.1364/ao.3.000187, 1964.

Deschamps, P.-Y., Breon, F.-M., Leroy, M., Podaire, A., Bricaud, A., Buriez, J.-C., and Seze, G.: The POLDER mission: instrument characteristics and scientific objectives, 32, 598–615, https://doi.org/10.1109/36.297978, 1994.

Diner, D. J., Xu, F., Garay, M. J., Martonchik, J. V., Rheingans, B. E., Geier, S., Davis, A., Hancock, B. R., Jovanovic, V. M., Bull, M. A., Capraro, K., Chipman, R. A., and McClain, S. C.: The Airborne Multiangle SpectroPolarimetric Imager (AirMSPI): a new tool for aerosol and cloud remote sensing, 6, 2007–2025, https://doi.org/10.5194/amt-6-2007-2013.

Emde, C., Buras-Schnell, R., Kylling, A., Mayer, B., Gasteiger, J., Hamann, U., Kylling, J., Richter, B., Pause, C., Dowling, T., and Bugliaro, L.: The libRadtran software package for radiative transfer calculations (version 2.0.1), 9, 1647–1672, https://doi.org/10.5194/gmd-9-1647-2016, 2016.

Ewald, F., Kölling, T., Baumgartner, A., Zinner, T., and Mayer, B.: Design and characterization of specMACS, a multipurpose hyperspectral cloud and sky imager, Atmospheric Measurement Techniques, 9, 2015–2042, https://doi.org/10.5194/amt-9-2015-2016, 2016.

Ewald, F., Groß, S., Hagen, M., Hirsch, L., Delanoë, J., and Bauer-Pfundstein, M.: Calibration of a 35 GHz airborne cloud radar: lessons learned and intercomparisons with 94 GHz cloud radars, 12, 1815–1839, https://doi.org/10.5194/amt-12-1815-2019, 2019.

Grandy, Jr, W. T.: Scattering of Waves from Large Spheres, Cambridge University Press, ISBN 9780521661263, https://doi.org/10.1017/CBO9780511524158, 2000.

Groß, S., Ewald, F., Stevens, B., Wirth, M., Dekoutsidis, G., Ehrlich, A., Kouklaki, D., Krüger, K., Rosenburg, S., Volkmer, L., von Bismark, J., Hirsch, L., Luebke, A. E., Marinou, E., Mayer, B., Pinol Sole, M., Wendisch, M., Windmiller, J., Amiridis, V., Koopman, R., Kubota, T., and Rapp, M.: Persistent EarthCARE underflight studies of the ITCZ and organized convection (PERCUSION): contribution to EarthCARE validation, 19, 3933–3959, https://doi.org/10.5194/amt-19-3933-2026, 2026.

Hansen, J. E.: Multiple Scattering of Polarized Light in Planetary Atmospheres Part II. Sunlight Reflected by Terrestrial Water Clouds, 28, 1400 – 1426, https://doi.org/10.1175/1520-0469(1971)028<1400:MSOPLI>2.0.CO;2, 1971.

Hansen, J. E. and Travis, L. D.: Light scattering in planetary atmospheres, 16, 527–610, https://doi.org/10.1007/bf00168069, 1974.

Hersbach, H., Bell, B., Berrisford, P., Hirahara, S., Horányi, A., Muñoz-Sabater, J., Nicolas, J., Peubey, C., Radu, R., Schepers, D., Simmons, A., Soci, C., Abdalla, S., Abellan, X., Balsamo, G., Bechtold, P., Biavati, G., Bidlot, J., Bonavita, M., Chiara, G., Dahlgren, P., Dee, D., Diamantakis, M., Dragani, R., Flemming, J., Forbes, R., Fuentes, M., Geer, A., Haimberger, L., Healy, S., Hogan, R. J., Hólm, E., Janisková, M., Keeley, S., Laloyaux, P., Lopez, P., Lupu, C., Radnoti, G., Rosnay, P., Rozum, I., Vamborg, F., Villaume, S., and Thépaut, J.-N.: The ERA5 global reanalysis, 146, 1999–2049, https://doi.org/10.1002/qj.3803, 2020.

Johnson, R. H., Rickenbach, T. M., Rutledge, S. A., Ciesielski, P. E., and Schubert, W. H.: Trimodal Characteristics of Tropical Convection, Journal of Climate, 12, 2397 – 2418, https://doi.org/10.1175/1520-0442(1999)012<2397:TCOTC>2.0.CO;2, 1999.

King, M. D., Platnick, S., Menzel, W. P., Ackerman, S. A., and Hubanks, P. A.: Spatial and Temporal Distribution of Clouds Observed by MODIS Onboard the Terra and Aqua Satellites, 51, 3826–3852, https://doi.org/10.1109/tgrs.2012.2227333, 2013.

Kölling, T., Zinner, T., and Mayer, B.: Aircraft-based stereographic reconstruction of 3-D cloud geometry, Atmospheric Measurement Techniques, 12, 1155–1166, https://doi.org/10.5194/amt-12-1155-2019, 2019.

Konow, H., Ewald, F., George, G., Jacob, M., Klingebiel, M., Kölling, T., Luebke, A. E., Mieslinger, T., Pörtge, V., Radtke, J., Schäfer, M., Schulz, H., Vogel, R., Wirth, M., Bony, S., Crewell, S., Ehrlich, A., Forster, L., Giez, A., Gödde, F., Groß, S., Gutleben, M., Hagen, M., Hirsch, L., Jansen, F., Lang, T., Mayer, B., Mech, M., Prange, M., Schnitt, S., Vial, J., Walbröl, A., Wendisch, M., Wolf, K., Zinner, T., Zöger, M., Ament, F., and Stevens, B.: EUREC ^{4} A's HALO, 13, 5545–5563, https://doi.org/10.5194/essd-13-5545-2021, 2021.

Krautstrunk, M. and Giez, A.: The Transition From FALCON to HALO Era Airborne Atmospheric Research, in: Atmospheric Physics, pp. 609–624, Springer Berlin Heidelberg, https://doi.org/10.1007/978-3-642-30183-4_37, 2012.

Liou, K.: Chapter 8 - Radiation and Climate, in: An Introduction to Atmospheric Radiation, vol. 84 of *International Geophysics*, pp. 442–521, Academic Press, https://doi.org/https://doi.org/10.1016/S0074-6142(02)80023-7, 2002.

Macke, A. and Großklaus, M.: Light scattering by nonspherical raindrops, 60, 355–363, https://doi.org/10.1016/s0022-4073(98)00011-9, 1998.

Marshall, J. S. and Palmer, W. M. K.: THE DISTRIBUTION OF RAINDROPS WITH SIZE, Journal of Atmospheric Sciences, 5, 165 – 166, https://doi.org/10.1175/1520-0469(1948)005<0165:TDORWS>2.0.CO;2, 1948.

Martins, J. V., Fernandez-Borda, R., McBride, B., Remer, L., and Barbosa, H. M. J.: The Harp Hype Ran Gular Imaging Polarimeter and the Need for Small Satellite Payloads with High Science Payoff for Earth Science Remote Sensing, in: IGARSS 2018 - 2018 IEEE International Geoscience and Remote Sensing Symposium, IEEE, https://doi.org/10.1109/igarss.2018.8518823, 2018.

Mayer, B. and Kylling, A.: Technical note: The libRadtran software package for radiative transfer calculations - description and examples of use, Atmospheric Chemistry and Physics, 5, 1855–1877, https://doi.org/10.5194/acp-5-1855-2005, 2005.

Mayer, B., Schröder, M., Preusker, R., and Schüller, L.: Remote sensing of water cloud droplet size distributions using the backscatter glory: a case study, 4, 1255–1263, https://doi.org/10.5194/acp-4-1255-2004, 2004.

McBride, B. A., Martins, J. V., Barbosa, H. M. J., Birmingham, W., and Remer, L. A.: Spatial distribution of cloud droplet size properties from Airborne Hyper-Angular Rainbow Polarimeter (AirHARP) measurements, 13, 1777–1796, https://doi.org/10.5194/amt-13-1777-2020, 2020.

Mech, M., Orlandi, E., Crewell, S., Ament, F., Hirsch, L., Hagen, M., Peters, G., and Stevens, B.: HAMP – the microwave package on the High Altitude and LOng range research aircraft (HALO), 7, 4539–4553, https://doi.org/10.5194/amt-7-4539-2014.

Mie, G.: Beiträge zur Optik trüber Medien, speziell kolloidaler Metallösungen, Annalen der Physik, 330, 377–445, https://doi.org/10.1002/andp.19083300302, 1908.

Miles, N. L., Verlinde, J., and Clothiaux, E. E.: Cloud Droplet Size Distributions in Low-Level Stratiform Clouds, Journal of the Atmospheric Sciences, 57, 295 – 311, https://doi.org/10.1175/1520-0469(2000)057<0295:CDSDIL>2.0.CO;2, 2000.

Mishchenko, M. I., Cairns, B., Hansen, J. E., Travis, L. D., Burg, R., Kaufman, Y. J., Martins, J. V., and Shettle, E. P.: Monitoring of aerosol forcing of climate from space: analysis of measurement requirements, 88, 149–161, https://doi.org/10.1016/j.jqsrt.2004.03.030, 2004.

Nakajima, T. and King, M. D.: Determination of the Optical Thickness and Effective Particle Radius of Clouds from Reflected Solar Radiation Measurements. Part I: Theory, 47, 1878–1893, https://doi.org/10.1175/1520-0469(1990)047<1878:dototo>2.0.co;2, 1990.

Pruppacher, H. and Klett, J.: Microphysics of Clouds and Precipitation, Springer Netherlands, ISBN 9780306481000, https://doi.org/10.1007/978-0-306-48100-0, 2010.

Pruppacher, H. R. and Beard, K. V.: A wind tunnel investigation of the internal circulation and shape of water drops falling at terminal velocity in air, 96, 247–256, https://doi.org/10.1002/qj.49709640807, 1970.

Pörtge, V., Kölling, T., Weber, A., Volkmer, L., Emde, C., Zinner, T., Forster, L., and Mayer, B.: High-spatial-resolution retrieval of cloud droplet size distribution from polarized observations of the cloudbow, Atmospheric Measurement Techniques, 16, 645–667, https://doi.org/10.5194/amt-16-645-2023, 2023.

Pörtge, V. T.: Understanding cloud droplet size distributions from multi-angle polarimetric observations, Ph.D. thesis, https://doi.org/10.5282/EDOC.34002, 2024.

Sadeghi, I., Munoz, A., Laven, P., Jarosz, W., Seron, F., Gutierrez, D., and Jensen, H. W.: Physically-based simulation of rainbows, 31, 1–12, https://doi.org/10.1145/2077341.2077344, 2012.

Shang, H., Chen, L., Bréon, F. M., Letu, H., Li, S., Wang, Z., and Su, L.: Impact of cloud horizontal inhomogeneity and directional sampling on the retrieval of cloud droplet size by the POLDER instrument, 8, 4931–4945, https://doi.org/10.5194/amt-8-4931-2015, 2015.

Shang, H., Letu, H., Bréon, F.-M., Riedi, J., Ma, R., Wang, Z., Nakajima, T. Y., Wang, Z., and Chen, L.: An improved algorithm of cloud droplet size distribution from POLDER polarized measurements, 228, 61–74, https://doi.org/10.1016/j.rse.2019.04.013, 2019.

Smith, R. E., McBride, B. A., Xu, X., Puthukkudy, A., Sienkiewicz, N., Cieslak, J. D., Remer, L. A., Fernandez-Borda, R., and Martins, J. V.: A new way to see the clouds: the hyper-angular rainbow polarimeter (HARP2) on the NASA PACE satellite mission, 6, https://doi.org/10.3389/frsen.2025.1710909, 2026.

Stevens, B., Ament, F., Bony, S., Crewell, S., Ewald, F., Gross, S., Hansen, A., Hirsch, L., Jacob, M., Kölling, T., Konow, H., Mayer, B., Wendisch, M., Wirth, M., Wolf, K., Bakan, S., Bauer-Pfundstein, M., Brueck, M., Delanoë, J., Ehrlich, A., Farrell, D., Forde, M., Gödde, F., Grob, H., Hagen, M., Jäkel, E., Jansen, F., Klepp, C., Klingebiel, M., Mech, M., Peters, G., Rapp, M., Wing, A. A., and Zinner, T.: A High-Altitude Long-Range Aircraft Configured as a Cloud Observatory: The NARVAL Expeditions, 100, 1061–1077, https://doi.org/10.1175/bams-d-18-0198.1, 2019.

Stevens, B., Bony, S., Farrell, D., Ament, F., Blyth, A., Fairall, C., Karstensen, J., Quinn, P. K., Speich, S., Acquistapace, C., Aemisegger, F., Albright, A. L., Bellenger, H., Bodenschatz, E., Caesar, K.-A., Chewitt-Lucas, R., de Boer, G., Delanoë, J., Denby, L., Ewald, F., Fildier, B., Forde, M., George, G., Gross, S., Hagen, M., Hausold, A., Heywood, K. J., Hirsch, L., Jacob, M., Jansen, F., Kinne, S., Klocke, D., Kölling, T., Konow, H., Lothon, M., Mohr, W., Naumann, A. K., Nuijens, L., Olivier, L., Pincus, R., Pöhlker, M., Reverdin, G., Roberts, G., Schnitt, S., Schulz, H., Siebesma, A. P., Stephan, C. C., Sullivan, P., Touzé-Peiffer, L., Vial, J., Vogel, R., Zuidema, P., Alexander, N., Alves, L., Arixi, S., Asmath, H., Bagheri, G., Baier, K., Bailey, A., Baranowski, D., Baron, A., Barrau, S., Barrett, P. A., Batier, F., Behrendt, A., Bendinger, A., Beucher, F., Bigorre, S., Blades, E., Blossey, P., Bock, O., Böing, S., Bosser, P., Bourras, D., Bouruet-Aubertot, P., Bower, K., Branellec, P., Branger, H., Brennek, M., Brewer, A., Brilouet, P.-E., Brügmann, B., Buehler, S. A., Burke, E., Burton, R., Calmer, R., Canonici, J.-C., Carton, X., Cato Jr., G., Charles, J. A., Chazette, P., Chen, Y., Chilinski, M. T., Choularton, T., Chuang, P., Clarke, S., Coe, H., Cornet, C., Coutris, P., Couvreux, F., Crewell, S., Cronin, T., Cui, Z., Cuypers, Y., Daley, A., Damerell, G. M., Dauhut, T., Deneke, H., Desbios, J.-P., Dörner, S., Donner, S., Douet, V., Drushka, K., Dütsch, M., Ehrlich, A., Emanuel, K., Emmanouilidis, A., Etienne, J.-C., Etienne-Leblanc, S., Faure, G., Feingold, G., Ferrero, L., Fix, A., Flamant, C., Flatau, P. J., Foltz, G. R., Forster, L., Furtuna, I., Gadian, A., Galewsky, J., Gallagher, M., Gallimore, P., Gaston, C., Gentemann, C., Geyskens, N., Giez, A., Gollop, J., Gouirand, I., Gourbeyre, C., de Graaf, D., de Groot, G. E., Grosz, R., Güttler, J., Gutleben, M., Hall, K., Harris, G., Helfer, K. C., Henze, D., Herbert, C., Holanda, B., Ibanez-Landeta, A., Intrieri, J., Iyer, S., Julien, F., Kalesse, H., Kazil, J., Kellman, A., Kidane, A. T., Kirchner, U., Klingebiel, M., Körner, M., Kremper, L. A., Kretzschmar, J., Krüger, O., Kumala, W., Kurz, A., L'Hégaret, P., Labaste, M., Lachlan-Cope, T., Laing, A., Landschützer, P., Lang, T., Lange, D., Lange, I., Laplace, C., Lavik, G., Laxenaire, R., Le Bihan, C., Leandro, M., Lefevre, N., Lena, M., Lenschow, D., Li, Q., Lloyd, G., Los, S., Losi, N., Lovell, O., Luneau, C., Makuch, P., Malinowski, S., Manta, G., Marinou, E., Marsden, N., Masson, S., Maury, N., Mayer, B., Mayers-Als, M., Mazel, C., McGeary, W., McWilliams, J. C., Mech, M., Mehlmann, M., Meroni, A. N., Mieslinger, T., Minikin, A., Minnett, P., Möller, G., Morfa Avalos, Y., Muller, C., Musat, I., Napoli, A., Neuberger, A., Noisel, C., Noone, D., Nordsiek, F., Nowak, J. L., Oswald, L., Parker, D. J., Peck, C., Person, R., Philippi, M., Plueddemann, A., Pöhlker, C., Pörtge, V., Pöschl, U., Pologne, L., Posyniak, M., Prange, M., Quiñones Meléndez, E., Radtke, J., Ramage, K., Reimann, J., Renault, L., Reus, K., Reyes, A., Ribbe, J., Ringel, M., Ritschel, M., Rocha, C. B., Rochetin, N., Röttenbacher, J., Rollo, C., Royer, H., Sadoulet, P., Saffin, L., Sandiford, S., Sandu, I., Schäfer, M., Schemann, V., Schirmacher, I., Schlenczek, O., Schmidt, J., Schröder, M., Schwarzenboeck, A., Sealy, A., Senff, C. J., Serikov, I., Shohan, S., Siddle, E., Smirnov, A., Späth, F., Spooner, B., Stolla, M. K., Szkółka, W., de Szoeke, S. P., Tarot, S., Tetoni, E., Thompson, E., Thomson, J., Tomassini, L., Totems, J., Ubele, A. A., Villiger, L., von Arx, J., Wagner, T., Walther, A., Webber, B., Wendisch, M., Whitehall, S., Wiltshire, A., Wing, A. A., Wirth, M., Wiskandt, J., Wolf, K., Worbes, L., Wright, E., Wulfmeyer, V., Young, S., Zhang, C., Zhang, D., Ziemen, F., Zinner, T., and Zöger, M.: EUREC^{4}A, Earth System Science Data, 13, 4067–4119, https://doi.org/10.5194/essd-13-4067-2021, 2021.

Stevens, B., Bony, S., Gross, S., Klocke, D., Windmiller, J. M., Wing, A. A., von Bismarck, J., Brito, E., David, R. O., Delanoë, J., Farrell, D., and Wu, Y.: ORCESTRA: Organized Convection and EarthCARE Studies Over the Tropical Atlantic, 79, 35–52, https://doi.org/10.16993/tellus.4123, 2026.

Tampieri, F. and Tomasi, C.: Size distribution models of fog and cloud droplets in terms of the modified gamma function, 28, 333–347, https://doi.org/10.1111/j.2153-3490.1976.tb00682.x, 1976.

Ulbrich, C. W.: Natural Variations in the Analytical Form of the Raindrop Size Distribution, 22, 1764–1775, https://doi.org/10.1175/1520-0450(1983)022<1764:nvitaf>2.0.co;2, 1983.

Volkmer, L., Kölling, T., Zinner, T., and Mayer, B.: Consideration of the cloud motion for aircraft-based stereographically derived cloud geometry and cloud top heights, 17, 6807–6817, https://doi.org/10.5194/amt-17-6807-2024, 2024a.

Volkmer, L., Pörtge, V., Jakub, F., and Mayer, B.: Model-based evaluation of cloud geometry and droplet size retrievals from two-dimensional polarized measurements of specMACS, 17, 1703–1719, https://doi.org/10.5194/amt-17-1703-2024, 2024b.

Weber, A., Kölling, T., Pörtge, V., Baumgartner, A., Rammeloo, C., Zinner, T., and Mayer, B.: Polarization upgrade of specMACS: calibration and characterization of the 2D RGB polarization-resolving cameras, 17, 1419–1439, https://doi.org/10.5194/amt-17-1419-2024, 2024.

Weber, A., Hoffmann, F., and Mayer, B.: Quasi-Lagrangian observations of cloud transitions during the initial phase of marine cold air outbreaks in the Arctic – Part 2: Vertical cloud structure, https://doi.org/10.5194/egusphere-2025-5832, 2025a.

Weber, A., Pörtge, V., Emde, C., and Mayer, B.: Retrieval of cloud thermodynamic phase partitioning from multi-angle polarimetric imaging of Arctic mixed-phase clouds, 18, 7581–7601, https://doi.org/10.5194/amt-18-7581-2025, 2025b.

Weber, A., Kirbus, B., Wendisch, M., and Mayer, B.: Quasi-Lagrangian observations of cloud transitions during the initial phase of marine cold air outbreaks in the Arctic - Part 1: Temporal and spatial evolution, 26, 3521–3540, https://doi.org/10.5194/acp-26-3521-2026, 2026.

Wendisch, M., Crewell, S., Ehrlich, A., Herber, A., Kirbus, B., Lüpkes, C., Mech, M., Abel, S. J., Akansu, E. F., Ament, F., Aubry, C., Becker, S., Borrmann, S., Bozem, H., Brückner, M., Clemen, H.-C., Dahlke, S., Dekoutsidis, G., Delanoë, J., De La Torre Castro, E., Dorff, H., Dupuy, R., Eppers, O., Ewald, F., George, G., Gorodetskaya, I. V., Grawe, S., Groß, S., Hartmann, J., Henning, S., Hirsch, L., Jäkel, E., Joppe, P., Jourdan, O., Jurányi, Z., Karalis, M., Kellermann, M., Klingebiel, M., Lonardi, M., Lucke, J., Luebke, A. E., Maahn, M., Maherndl, N., Maturilli, M., Mayer, B., Mayer, J., Mertes, S., Michaelis, J., Michalkov, M., Mioche, G., Moser, M., Müller, H., Neggers, R., Ori, D., Paul, D., Paulus, F. M., Pilz, C., Pithan, F., Pöhlker, M., Pörtge, V., Ringel, M., Risse, N., Roberts, G. C., Rosenburg, S., Röttenbacher, J., Rückert, J., Schäfer, M., Schaefer, J., Schemann, V., Schirmacher, I., Schmidt, J., Schmidt, S., Schneider, J., Schnitt, S., Schwarz, A., Siebert, H., Sodemann, H., Sperzel, T., Spreen, G., Stevens, B., Stratmann, F., Svensson, G., Tatzelt, C., Tuch, T., Vihma, T., Voigt, C., Volkmer, L., Walbröl, A., Weber, A., Wehner, B., Wetzel, B., Wirth, M., and Zinner, T.: Overview: quasi-Lagrangian observations of Arctic air mass transformations – introduction and initial results of the HALO–(AC) 3 aircraft campaign, 24, 8865–8892, https://doi.org/10.5194/acp-24-8865-2024, 2024.

Werdell, P. J., Cairns, B., Caplan, S. A., Cetinić, I., Foley, S. R., Franz, B. A., Gao, M., Fasnacht, Z. T., Huemmrich, K. F., Ibrahim, A., Knobelspiesse, K. D., Mannino, A., McKinna, L. I. W., Poulin, C., Rajapakshe, C., and Sayer, A. M.: Advancing Earth System Science With the <scp>NASA</scp> Plankton, Aerosol, Cloud, Ocean Ecosystem (<scp>PACE</scp>) Satellite Mission, 32, https://doi.org/10.1111/gcb.70869, 2026.

Willis, P. T. and Tattelman, P.: Drop-Size Distributions Associated with Intense Rainfall, 28, 3–15, https://doi.org/10.1175/1520-0450(1989)028<0003:dsdawi>2.0.co;2, 1989.

Wirth, M. and Groß, S.: WALES lidar data from the PERCUSION field campaign for the Barbados period Version 1.2, https://doi.org/10.5281/ZENODO.17153149, 2025.

Wirth, M., Fix, A., Mahnke, P., Schwarzer, H., Schrandt, F., and Ehret, G.: The airborne multi-wavelength water vapor differential absorption lidar WALES: system design and performance, 96, 201–213, https://doi.org/10.1007/s00340-009-3365-7, 2009.

Wiscombe, W. J.: Improved Mie scattering algorithms, Appl. Opt., 19, 1505–1509, https://doi.org/10.1364/AO.19.001505, 1980.

Xu, F., Harten, G., Diner, D. J., Davis, A. B., Seidel, F. C., Rheingans, B., Tosca, M., Alexandrov, M. D., Cairns, B., Ferrare, R. A., Burton, S. P., Fenn, M. A., Hostetler, C. A., Wood, R., and Redemann, J.: Coupled Retrieval of Liquid Water Cloud and Above-Cloud Aerosol Properties Using the Airborne Multiangle SpectroPolarimetric Imager (AirMSPI), 123, 3175–3204, https://doi.org/10.1002/2017jd027926.